

RESEARCH ARTICLE

A WDR47 homolog facilitates ciliogenesis by modulating intraflagellar transport

Chun-Xue Song^{1,2}, Xian-Ting Zeng³, Wan-Xin Zeng³, Rong Liu^{1,2}, Xia-Jing Tong^{3,*} and Qian Li^{1,2,4,*}

ABSTRACT

Cilia are conserved organelles found in many cell types in eukaryotes, and their dysfunction causes defects in environmental sensing and signaling transduction; such defects are termed ciliopathies. Distinct cilia have cell-specific morphologies and exert distinct functions. However, the underlying mechanisms of cell-specific ciliogenesis and regulation are unclear. Here, we identified a WD40-repeat (WDR) protein, NMTN-1 (the homolog of mammalian WDR47), and show that it is specifically required for ciliogenesis of AWB chemosensory neurons in *C. elegans*. NMTN-1 is expressed in the AWB chemosensory neuron pair, and is enriched at the basal body (BB) of the AWB cilia. Knockout of *nmtn-1* causes abnormal AWB neuron cilia morphology, structural integrity, and induces aberrant AWB-mediated aversive behaviors. We further demonstrate that *nmtn-1* deletion affects movement of intraflagellar transport (IFT) particles and their cargo delivery in AWB neurons. Our results indicate that NMTN-1 is essential for AWB neuron ciliary morphology and function, which reveal a novel mechanism for cell-specific ciliogenesis. Given that WDR47/NMTN-1 is conserved in mammals, our findings may help understanding of the process of cell-specific ciliogenesis and provide insights for treating ciliopathies.

KEY WORDS: Cilia, Chemosensory neuron, WD40-repeat protein, Intraflagellar transport

INTRODUCTION

Cilia are microtubule-based sensory organelles that are found throughout most eukaryotes (Pedersen et al., 2012). They play essential roles in diverse physiological and developmental processes, including transduction of environmental signals, establishing cell polarity, modulation of cellular motility and regulating fluid flow (Berbari et al., 2009; Bloodgood, 2010; Dasgupta and Amack, 2016; Goetz and Anderson, 2010; Pan et al., 2005; Ringers et al., 2020). Dysfunction of cilia underlies a wide range of human syndromes – termed ciliopathies – that feature diverse phenotypes, including brain malformation, infertility, renal cyst formation, retinal degeneration and anosmia (loss of smell)

(Brown and Witman, 2014; Jenkins et al., 2009; Reiter and Leroux, 2017; Sharma et al., 2008; Uytingco et al., 2019a).

Cilia comprise three major compartments – the basal body (BB) with fibrous apparatuses transition fibers and basal feet, the transition zone (TZ), and the microtubule-based ciliary scaffold known as an ‘axoneme’ (Kobayashi and Dynlacht, 2011; Reiter et al., 2012; Wei et al., 2015). Cilia are nucleated by the BB (derived from the mother centriole) and eventually protrude from the cell surface (Ishikawa and Marshall, 2011). Subsequently, the TZ is templated to gate ciliary protein trafficking (Williams et al., 2011). Known ciliary cargoes include cilia structural components, G-protein-coupled receptors, ion channels and other signaling molecules (Inglis et al., 2007; Lehtreck, 2015; Nachury, 2018). Those cargoes are transported bi-directionally along the axoneme via a process called intraflagellar transport (IFT) (Hao and Scholey, 2009). IFT components are recruited to elongate the ciliary axoneme. The IFT machinery consists of kinesin-2 and IFT dynein motors, together with the IFT-A and the IFT-B cargo adaptor complexes, which mediate the bidirectional movement of IFT cargoes along the axoneme (Hao and Scholey, 2009; Jordan and Pigino, 2021). The anterograde IFT motors of the kinesin-2 family transports IFT particles from the cilia base to the cilia tip for incorporation into ciliary structures, whereas the retrograde IFT motors of dynein recycle kinesin-2 and IFT particles back to the cilia base (Hao and Scholey, 2009; Prevo et al., 2017). In addition, the Bardet–Biedl syndrome (BBS) proteins are required to stabilize the association of IFT motors and IFT particles (Ou et al., 2005; Uytingco et al., 2019b). This bidirectional cargo transport is essential for ciliogenesis (Ishikawa and Marshall, 2011). It has been reported that impairment of IFT leads to defects in cilia structure and function across different species. In *C. elegans*, mutations in IFT particle genes and motor genes have been shown to alter the cilia morphology of chemosensory neurons (Mukhopadhyay et al., 2007). Inactivation of the IFT component IFT88 results in shortened cilia in a mouse model of polycystic kidney disease (Shao et al., 2020). In addition, loss of BBS proteins leads to disorganization of the dendritic microtubule network of olfactory cilia and causes anosmia in mice (Kulaga et al., 2004).

Although the basic assembly mechanisms and structures of cilia are highly conserved, it is clear that these structures exhibit distinct lengths and morphologies depending on the identity and condition of the cells they are generated within; it is also clear that specialized cilia exert unique functional roles (Silverman and Leroux, 2009). For example, the multiciliated protist model *Tetrahymena* carries two types of cilia (oral and locomotory), which exhibit asymmetries in the anterior-posterior and left-right axes (Soares et al., 2019). These two types of cilia have different mechanisms to control cilia oscillation and to sense viscosity (Jung et al., 2014). In mammals, cilia of mammalian olfactory sensory neurons are known to have different lengths in distinct regions of the olfactory epithelium (Challis et al., 2015); olfactory sensory neurons situated in the

¹Songjiang Institute and Songjiang Hospital, Shanghai Jiao Tong University School of Medicine, Shanghai 201600, China. ²Department of Anatomy and Physiology, Ministry of Education-Shanghai Key Laboratory of Children's Environmental Health in Xinhua Hospital, Shanghai Jiao Tong University School of Medicine, Shanghai, 200025, China. ³School of Life Science and Technology, ShanghaiTech University, Shanghai 201210, China. ⁴Shanghai Research Center for Brain Science and Brain-Inspired Intelligence, Shanghai 201210, China.

*Authors for correspondence (tongxj@shanghaitech.edu.cn; liqian@shsmu.edu.cn)

DOI: C.-X.S., 0000-0001-7384-3939; X.-T.Z., 0000-0001-5705-2782; X.-J.T., 0000-0001-5634-1136; Q.L., 0000-0003-1300-3377

Handling Editor: Guangshuo Ou
Received 6 June 2022; Accepted 21 November 2022

anterior areas have longer cilia and are more sensitive to odorants than those in the posterior regions (Challis et al., 2015). These findings make it clear that cilia identity (including morphology and function) is under strict control. However, mechanisms through which the unique genesis, structural maintenance and/or function of such cell-specific cilia remain elusive.

C. elegans has been repeatedly used as a model system to explore mechanisms regulating cell-specific cilia morphology and function (Bae and Barr, 2011; Inglis et al., 2007; Ou et al., 2007). *C. elegans* has exactly 60 ciliated cells, with variable morphology and function (Bargmann, 2006). Among the ciliated neurons, AWA, AWB, AWC, ASH and ADL neurons belong to chemosensory neurons, enabling worms to detect a wide variety of volatile (olfactory) and water-soluble (gustatory) cues associated with food and danger (Bargmann, 2006; Emily et al., 1997; Hart and Chao, 2010; Li and Liberles, 2015; Qian et al., 2021; Yoshida et al., 2012). Regarding morphology, AWA, AWB, and AWC neurons have ‘wing’ cilia with distinct wing-like morphologies, whereas the ASH and ADL neurons have ‘channel’ cilia with rod-like shapes (Inglis et al., 2007). For odorant recognition, the AWA and AWC neuron pairs detect volatile attractants (Cornelia et al., 1993; Sengupta, 2007), whereas ASH, ADL and AWB neurons respond to volatile repellants (Chao et al., 2004; Sengupta, 2007). Thus, the cilia of particular chemosensory neurons of *C. elegans* represent an excellent model system to explore the cell-specific regulation of cilia morphology and function.

The WD40-repeat (WDR) protein family is a large group of proteins containing the WDR motifs comprised of ~40 amino acids terminating in tryptophan (W) and aspartic acid (D) (Kim and Kim, 2020). At least 17 different WDR proteins are associated with ciliopathies and the majority of them have been identified as IFT components. One of the WDR proteins, WDR47 has been implicated in regulating formation of the central pair microtubules and ciliary beat in the motile cilia (Liu et al., 2021). However, its function in the primary cilia, such as the chemosensory neurons remains unknown. Given that WDR47 is highly conserved with NMTN-1 as the homolog in *C. elegans*, we set out to investigate whether NMTN-1 regulates the function of specific chemosensory neurons in *C. elegans*.

Here, we discovered that NMTN-1 is required for AWB-mediated avoidance behaviors. After showing that NMTN-1 is expressed in the AWB neuron pair and is enriched at the BB of AWB cilia, we demonstrate that knockout of *nmtn-1* affects the cilia length and morphology of the AWB neurons as well as AWB-mediated chemosensation. To explain these mutant phenotypes, our data support that NMTN-1 helps to maintain appropriate IFT motor movement and proper IFT cargo delivery. In all, our results indicate that NMTN-1 participates in the ciliogenesis via IFT particle movement in a cell-specific manner. Given that WDR47/NMTN-1 is conserved in mammals, the mechanism we identified here may help us to better understand the process of cell-specific ciliogenesis and molecular mechanism for cilia identity.

RESULTS

NMTN-1 is expressed in the AWB chemosensory neuron pair

To examine the expression pattern of NMTN-1 in *C. elegans*, we generated transgenic animals expressing GFP under the *nmtn-1* promoter. We detected the strong GFP signals in both the ciliated amphid and phasmid neurons (Fig. 1A; Table 1). Next, we focused on the amphid chemosensory neurons and asked whether NMTN-1 is expressed in specific chemosensory neurons. There are five pairs of chemosensory neurons (olfactory) that detect volatile odors (Hart and Chao, 2010). AWA and AWC neurons respond to volatile

attractants (Cornelia et al., 1993; Sengupta, 2007), whereas ASH, ADL and AWB neurons respond to volatile repellants (Chao et al., 2004; Sengupta, 2007). We labeled the individual chemosensory neuron pairs by expressing mCherry under neuron-type specific promoters (*odr-10* promoter for AWA, *str-1* promoter for AWB, *str-2* promoter for AWC, and *srb-6* promoter for ASH and ADL). We found strong GFP signals in the AWB neurons but not AWA or ASH and ADL neurons, and found a dim GFP signal in the AWC neurons (Fig. 1B,C). These data show that NMTN-1 is expressed in the AWB chemosensory neuron pair known to function in chemosensation and aversion behaviors (Emily et al., 1997).

NMTN-1 is enriched at the BB of cilia

To study the subcellular localization of NMTN-1 in AWB neurons, we constructed a mNeonGreen-NMTN-1 (mNG::NMTN-1) fusion protein with expression under the control of the *nmtn-1* promoter (*Pnmtn-1*). The mNeonGreen signals were observed at the cilia and cell body of AWB neurons. Furthermore, although NMTN-1 was found throughout the cilia, it was more enriched at the base of the cilia (Fig. 1D,F–G). This localization pattern was observed in all of the analyzed animals. Interestingly, mNG::NMTN-1 appears to show a punctate pattern in the dendrites with unknown vesicular identity (Fig. 1D). We also constructed a C-terminal-tagged NMTN-1-mNeonGreen (NMTN-1::mNG) fusion protein (same promoter), and found a similar localization pattern to that for the N-terminal-tagged mNG::NMTN-1 (Fig. 1E). We also investigated the expression pattern of NMTN-1 at different developmental stages using the *Pnmtn-1*::mNG::NMTN-1 fusion protein, and found that NMTN-1 was expressed in the cilia of the AWB neurons from egg to adult (day 4) (Fig. S1A,B).

There are two substructures at the base of cilia known to affect ciliogenesis and control ciliary protein composition – the BB and the TZ (Fig. 1H) (Reiter et al., 2012). Cilia are nucleated by the BB, and beyond the BB lies the TZ, which acts as a ‘gate’ to regulate the IFT-dependent trafficking of ciliary proteins to and from cilia (Ishikawa and Marshall, 2011). To detect whether NMTN-1 is expressed in the BB and/or TZ, we labeled these substructures with mCherry-tagged MKS-5 and DYF-19 (Nechipurenko et al., 2016; Wei et al., 2013). NMTN-1 was colocalized with DYF-19 but not MKS-5 (Fig. 1F–I), suggesting that NMTN-1 is localized at the BB of the cilia of AWB neurons. The localization of NMTN-1 in the BB implies that NMTN-1 might regulate the BB structure. To test this possibility, we examined the distribution of mCherry-tagged DYF-19 proteins in *nmtn-1* mutants. No abnormal localization of DYF-19 proteins was observed in *nmtn-1* mutants, indicating that loss of NMTN-1 might not affect the localization of ciliary base proteins (Fig. S1C).

nmtn-1 mutation causes morphology defects of AWB cilia

Given that the BB is known to function as a nucleation site for cilia biogenesis (Marshall, 2008), we wondered whether NMTN-1 might participate in the morphology of the AWB wing cilia. We classified the AWB cilia phenotypes into three categories using a previously reported method of quantifying AWB cilia morphologies (Olivier-Mason et al., 2013). Briefly, category 1 cilia have characteristic Y-shaped morphology with two primary branches and no fans. Category 2 cilia have enlarged fans along the primary branches. Category 3 cilia have more than one secondary branch emanating from the primary branch (Fig. 2A). We quantified the percentage of cilia in each of three categories in wild-type (WT) and *nmtn-1* mutants, and found that the percentage of category 1 cilia was significantly increased in *nmtn-1* mutants, whereas the percentage of category 2 cilia was significantly decreased in these animals

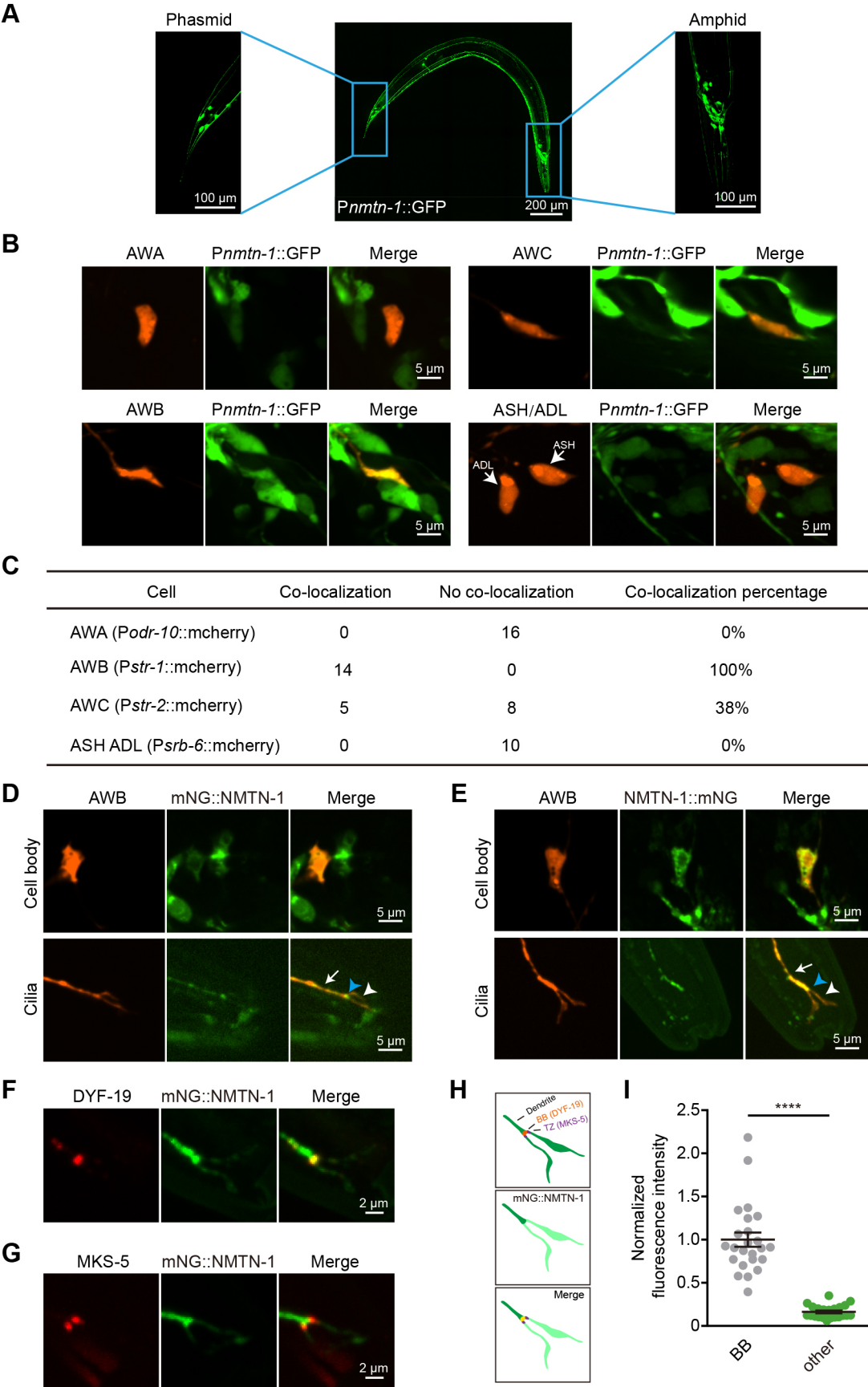


Fig. 1. See next page for legend.

Fig. 1. NMTN-1 is expressed in the AWB chemosensory neuron pair and enriched in the BB region. (A) NMTN-1 is expressed in the amphids and phasmids of *C. elegans*. The left and right images are enlarged views of the phasmids and amphids, respectively. (B) Representative images of *Pnmtn-1::GFP* signals in five pairs of olfactory neurons. The AWA, AWB and AWC neurons are marked by *Podr-10::mCherry*, *Pstr-1::mCherry*, and *Pstr-2::mCherry*. The ASH and ADL neurons are marked by *Pstrb-6::mCherry*. (C) Quantification colocalization of *Pnmtn-1::GFP* signals in five pairs of olfactory neurons. (D) Representative images showing *Pnmtn-1::mNG::NMTN-1* signals. The AWB neurons were visualized via expression of *Pstr-1::mCherry*. White arrowhead, blue arrowhead, and white arrow indicate cilia, the cilia base and dendrites, respectively. (E) Representative images showing *Pnmtn-1::NMTN-1::mNG* signals. The AWB neurons were marked by expression of *Pstr-1::mCherry*. White arrowhead, blue arrowhead, and white arrow indicate cilia, cilia base, and dendrites, respectively. (F) Colocalization of *Pstr-1::mNG::NMTN-1* and the BB (*Pstr-1::DYF-19::mCherry*) marker. (G) Colocalization of *Pstr-1::mNG::NMTN-1* and the TZ (*Pstr-1::MKS-5::mCherry*) marker. (H) Cartoon illustration of expression pattern of *Pstr-1::mNG::NMTN-1* in the transition zone (TZ) and basal body (BB) of the AWB cilia. MKS-5 and DYF-19 are markers for the TZ and the BB, respectively. (I) Quantification of the fluorescence intensities of *Pstr-1::mNG::NMTN-1* in BB and other parts of the cilia. Each cilium analyzed is represented by a dot. Data are presented as mean±s.e.m. $n=24$. **** $P<0.0001$ (unpaired two-tailed Student's *t*-test). Images shown in A,B,D–G are representative of at least 10 repeats.

(Fig. 2B). We also measured the length of the AWB cilia – the typical AWB cilia contain two primary branches with unequal lengths, and we found that the lengths of both long and short branches in *nmtn-1* mutants were significantly shorter than in WT (Fig. 2C). These results collectively support that NMTN-1 regulates the cilia morphology of the AWB neurons.

As we observed above that there was a dim NMTN-1 signal in AWC neurons (Fig. 1B), we therefore examined AWC cilia morphology in *nmtn-1* mutants. An abnormal morphology with a discrete fan-shape cilia structure was occasionally observed in *nmtn-1* mutants (16% in *nmtn-1* mutants versus 0% in WT; Fig. S2A,B). However, there were no significant differences in the AWC cilia area between *nmtn-1* mutants and WT animals (Fig. S2C). We also investigated whether NMTN-1 is required to maintain cilia morphology in other cell types using OSM-6::GFP fusion proteins to label cilia in all amphid ciliated sensory neurons. We found no significant changes in overall cilia length in *nmtn-1* mutants in cells other than the AWB neurons (Fig. S2D,E).

***nmtn-1* mutation causes structural integrity defects of AWB cilia**

We also performed a Dil dye-filling experiment – which is routinely used to validate the structural integrity of cilia (Tong and Burglin, 2010) – to assess the specific impacts of NMTN-1 in maintaining the AWB cilia structural integrity. After 30 min of Dil exposure, we analyzed the fluorescence intensity of Dil in the cell body. The dye signal in the AWB neurons of *nmtn-1* mutants was significantly dimmer than in the WT (Fig. 2D,E), suggesting apparent structural integrity defects in the mutant AWB cilia. In contrast, no Dil absorption defects were observed in other neurons (Fig. 2F). Furthermore, the Dil dye absorption defects in the AWB neurons of *nmtn-1* mutants were restored upon the specific expression of NMTN-1 in the AWB neurons driven by the *str-1* promoter (Fig. 2D,E). These data suggest that NMTN-1 functions to maintain the structural integrity of the AWB neuron cilia.

NMTN-1 is required for AWB-mediated aversion behaviors

The abnormal cilia morphology we detected in the AWB neurons of *nmtn-1* mutants prompted us to test whether NMTN-1 is required

Table 1. Summary of the neurons that express NMTN-1

	Cell type	Localization	Expression	TPM in scRNA-seq (Taylor et al., 2021)
1	PVT	Tail	Yes	433.525
2	PDE	Body	Yes	195.906
3	LUA	Tail	Yes	178.6
4	DVB	Tail	Yes	134.824
5	PQR	Tail	Yes	128.286
6	OLL	Head	Yes	125.345
7	SAB	Head	Yes	97.664
8	ALN	Tail	Yes	92.792
9	HSN	Body	Yes	88.634
10	AWB	Head	Yes	85.874
11	PDB	Tail	Yes	62.057
12	ALM	Body	Yes	55.923
13	AVK	Head	Yes	47.163
14	AFD	Head	Yes	39.668
15	SAA	Head	uncertain	315.199
16	OLQ	Head	uncertain	170.023
17	AVL	Head	uncertain	153.126
18	URY	Head	uncertain	129.345
19	RMH	Head	uncertain	128.242
20	DB01	Body	uncertain	123.899
21	VA	Body	uncertain	121.969
22	AUA	Head	uncertain	108.363
23	DB	Body	uncertain	105.334
24	VD_DD	Body	uncertain	105.185
25	VB	Body	uncertain	101.113
26	AVJ	Head	uncertain	96.854
27	AVG	Head	uncertain	94.878
28	AQR	Head	uncertain	93.88
29	M2	Head	uncertain	92.326
30	ASER	Head	uncertain	83.318
31	RMG	Head	uncertain	81.731
32	ASK	Head	uncertain	80.329
33	AVA	Head	uncertain	79.898
34	VB02	Body	uncertain	79.759
35	DA	Body	uncertain	78.043
36	AVF	Head	uncertain	74.801
37	AVB	Head	uncertain	67.841
38	VB01	Body	uncertain	66.206
39	ASG	Head	uncertain	65.33
40	RMD_DV	Head	uncertain	61.769

The data for the transcripts per kilobase million (TPM) of *nmtn-1* in scRNA-seq is from Taylor et al., 2021.

for the AWB-mediated chemosensation behaviors. The AWB neurons are known to mediate aversion behaviors in response to odorants such as 2-nonanone, and these responses require intact and functional cilia (Emily et al., 1997; Hart and Chao, 2010). We conducted a classic chemotaxis assay to examine aversion behavior to 2-nonanone (Fig. 3A). Briefly, 9 cm plates containing regular nematode growth medium (NGM) were spotted with control (ethanol) or 2-nonanone on opposite sides, and the paralysis agent sodium azide was added immediately before the addition of worms in the center of the plates (Fig. 3A). In line with the previous report (Cornelia et al., 1993), we observed that WT animals were repelled by 2-nonanone and thus had a negative chemotaxis index value. The chemotaxis index value was significantly increased in the *nmtn-1* mutants (Fig. 3B). Furthermore, restoring NMTN-1 expression either in the NMTN-1-expressing neurons (under the *nmtn-1* promoter) or in the AWB neurons (under the AWB-specific *str-1* promoter) rescued the chemotaxis defects (Fig. 3B). We also observed an impaired aversion response to octanol in the *nmtn-1* mutants; octanol is known to act on a group of neurons including AWB (Fig. 3C) (Chao et al., 2004). Restoring NMTN-1 expression

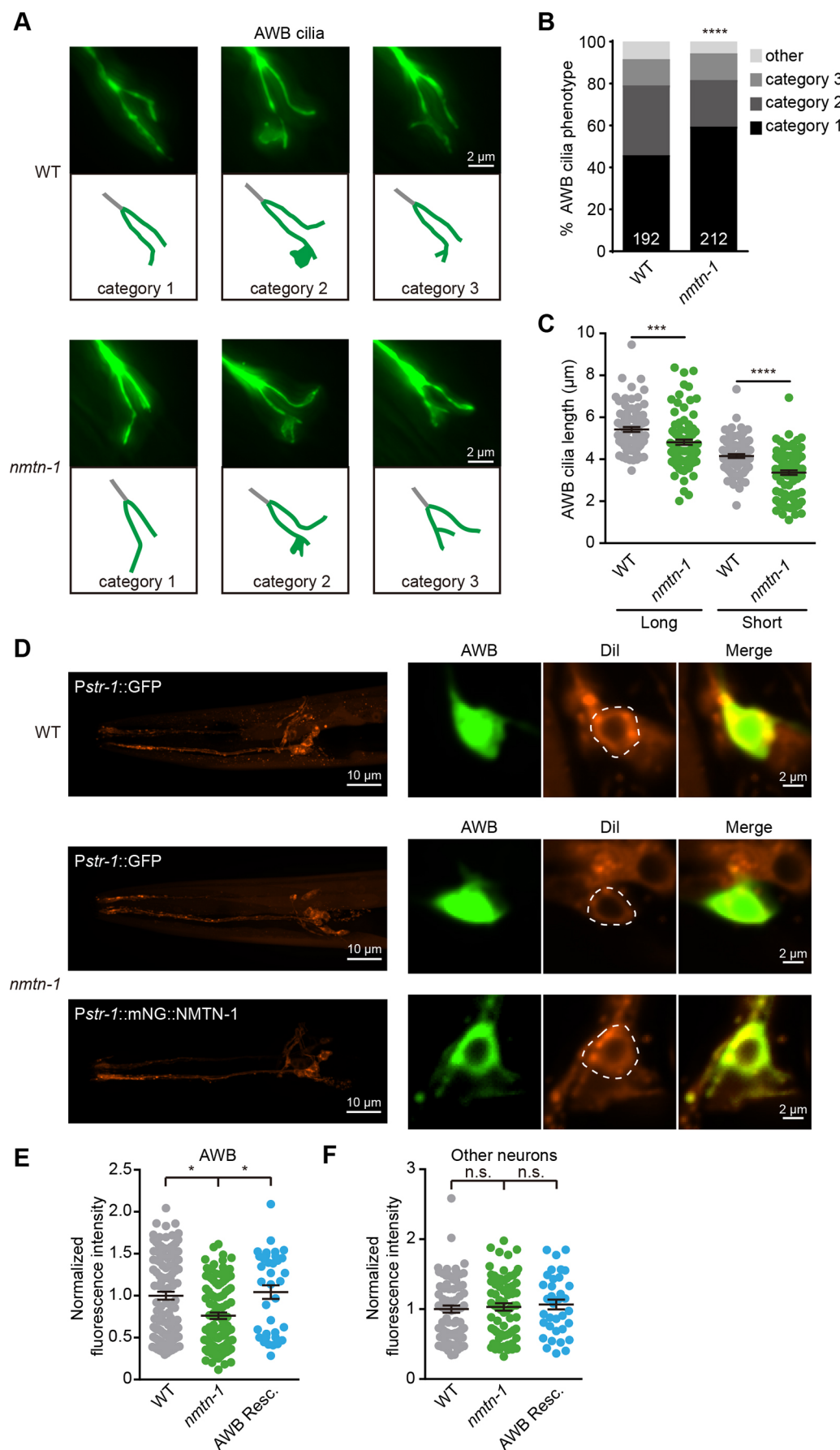


Fig. 2. See next page for legend.

Fig. 2. *nmtn-1* mutants exhibit defects in the AWB cilia morphology.

(A) Representative images of the AWB cilia in three categories according to cilia morphology in WT and *nmtn-1* mutants. Cilia were visualized using the *Pstr-1::GFP* marker, and were classified into the three categories according to the cilia morphology. (B) Percentage of the AWB cilia in three categories in WT and *nmtn-1* mutants (*n* values are given on the graph). (C) Quantification of the cilia length of the AWB neurons in WT and *nmtn-1* mutants. Each cilium analyzed is represented by a dot. *n*=82 for WT and *n*=95 for *nmtn-1* mutants. Data are presented as mean±s.e.m. (D–F) The *nmtn-1* mutants exhibited cell-specific defects in uptake of the lipophilic dye Dil. Representative images of Dil uptake in amphid sensory neurons in WT and mutants are displayed. The dotted lines represent AWB neurons (D). The dye-filling defect in AWB neurons of *nmtn-1* animals was rescued by expression of *Pstr-1::mNG::NMTN-1* (E). In contrast, the dye uptake in other neurons (random dye-filled non-AWB neurons) was normal in *nmtn-1* mutants (F). Each neuron analyzed is represented by a dot. *n*=115 for WT, *n*=104 for *nmtn-1* mutants, and *n*=36 for AWB rescue in E. *n*=76 for WT, *n*=70 for *nmtn-1* mutants, and *n*=36 for AWB rescue in F. Data are presented as mean±s.e.m., **P*<0.05; ****P*<0.001; *****P*<0.0001; n.s. not significant [Chi-squared test (B); unpaired two-tailed Student's *t*-test (C,E,F)].

in the NMTN-1-expressing neurons (under the *nmtn-1* promoter) rescued the chemotaxis defects (Fig. 3C). No effects were observed when we investigated the attraction behaviors to different dilutions of diacetyl, which is mediated by the AWA neuron (Fig. 3D) (Cornelia et al., 1993). We did observe an impaired AWC-mediated attraction response to isopentyl alcohol in *nmtn-1* mutants (Fig. 3E) (Cornelia et al., 1993), which might be due to the lower level of NMTN-1 in the AWC neurons (Fig. 1B). Collectively, our data support the notion that NMTN-1 functions in the AWB neurons to participate in the chemosensation behavior.

The overall ultrastructure of AWB cilia is not severely affected by *nmtn-1* mutation

To explore the mechanisms underlying the impact of NMTN-1 on ciliogenesis, we probed the ultrastructure of amphid cilia using scanning electron microscopy (SEM) (Serwas and Dammermann, 2015). Unlike the axonemes of channel cilia, the microtubules in the AWB cilia lack an obvious organization (Doroquez et al., 2014). We did not detect any microtubules in the distal segments of the AWB cilia, yet we did note the presence of singlet microtubules in the proximal segments. However, no obvious abnormalities of the axoneme structure were observed in *nmtn-1* mutants (Fig. S3A). In addition, the number of microtubules in the channel cilia and the AWB cilia did not differ significantly between WT and *nmtn-1* mutants (Fig. S3B,C). There was also no significant change in the number of open B tubule breaks identified in previous reports (Fig. S3D) (Jauregui et al., 2008; O'Hagan et al., 2011). Together, those results suggest no significant disruption of the overall ultrastructure of AWB cilia after deletion of *nmtn-1*. However, we could not completely rule out the possibility that NMTN-1 regulates some aspects of the cilia structure, such as the 3D organization of microtubules as previously reported (Ma et al., 2019; Schouteden et al., 2015; Silva et al., 2017).

***nmtn-1* mutation perturbs the velocity distributions of IFT components**

Ciliogenesis and cilia structure require the IFT-mediated bidirectional transport of particles along the microtubules (Hao and Scholey, 2009), so we examined whether deletion of *nmtn-1* influences IFT particle movement. In *C. elegans*, two members of the kinesin-2 family, heterotrimeric kinesin-II (including KAP-1 protein) and homodimeric OSM-3 cooperate to form two sequential

anterograde IFT pathways that build distinct parts of cilia (Scholey, 2008). IFT particles involve two subcomplexes – IFT-A and IFT-B. In *C. elegans*, IFT-A associates with kinesin-II to form the IFT-A subcomplex, and IFT-B associates with OSM-3 to form the IFT-B subcomplex. In addition, the two subcomplexes are coupled by BBS proteins to move together during anterograde transport. In BBSome mutants, IFT-A–kinesin-II and IFT-B–OSM-3 sub-complexes are dissociated and move separately (Hao and Scholey, 2009; Liang et al., 2014; Prevo et al., 2017). To specifically examine IFT movement in the AWB neurons (Brust-Mascher et al., 2013), we expressed an mNG reporter fusion variant of the KAP-1 and OSM-3 motor proteins, and the IFT-B complex subunit OSM-6 in the AWB neuron pair (under the AWB-specific *str-1* promoter) (Fig. S4A). In the AWB cilia of WT animals, the velocity of OSM-3 (0.87 µm/s) was a bit faster than that of KAP-1 and OSM-6 (0.64 µm/s and 0.63 µm/s) in the middle segments (Fig. 4A, Table 2). This is possibly because some OSM-3 motors move alone in the middle segments, which is consistent with previous reports (Mukhopadhyay et al., 2007). Interestingly, the velocity of OSM-3 (0.94 µm/s) was increased in the AWB cilia middle segments of *nmtn-1* mutants, whereas the velocity of OSM-6 (0.53 µm/s) was decreased in *nmtn-1* mutants (Fig. 4A, Table 2). We did not observe changes in the velocity of KAP-1. We hypothesized that some kinesin-II–OSM-3–OSM-6 complexes were dissociated in *nmtn-1* mutants. As a result, more separate OSM-3 would be released to cause increased average velocity of OSM-3. By contrast, OSM-6 could be retained with kinesin-II to cause decreased average velocity of OSM-6 (Fig. 4C). To further test this hypothesis, we generated three double mutant animals and performed time-lapse imaging experiments on OSM-6 movement (Fig. 4B). In *kap-1;nmtn-1* double mutants, the velocity of OSM-6 was increased to 1.09 µm/s, which is similar to the velocity of OSM-3 alone. In *osm-3;nmtn-1* double mutants, OSM-6 moved at 0.55 µm/s, which is similar to the velocity of kinesin-II alone. In *bbs-8;nmtn-1* double mutants, kinesin-II and OSM-3 were dissociated as previously reported. In this case, OSM-6 is transported by kinesin-II and OSM-3 separately, which is consistent with a mean movement speed of 0.70 µm/s (Ou et al., 2005). Those data indicate that loss of *nmtn-1* perturbs the velocity distributions of IFT components. As controls, we did not detect significant changes in IFT velocities in the ASH or ADL cilia (under the *srb-6* promoter) (Table 2), further suggesting that NMTN-1 is important for proper IFT movement in the AWB cilia.

To examine whether NMTN-1 is an IFT component or otherwise physically associates with the IFT machinery, we analyzed the mobility of NMTN-1 by making kymographs; neither anterograde nor retrograde movement was observed in the cilia or dendrites (Fig. S4B,C), indicating that the observed regulatory impacts of NMTN-1 knockout on IFT movement might result from indirect interactions with IFT machinery.

***nmtn-1* mutation might alter IFT cargo localization**

Given that NMTN-1 is required for IFT particle movement, we next examined whether IFT cargo transport requires NMTN-1. As an IFT cargo, TAX-4 is a cyclic nucleotide-gated channel protein localized on the cilia membrane that participates in the olfactory signaling pathway (Bargmann, 2006; Coburn and Bargmann, 1996). We studied the subciliary localization of TAX-4 in the *nmtn-1* mutants. We expressed a TAX-4::sfGFP fusion protein in the AWB neurons (under the *str-1* promoter) and found that TAX-4 was localized in the cilia in all of the WT animals. In contrast, TAX-4 was mislocalized to the base of cilia in 20–30% of *nmtn-1* mutants (Fig. S5A–C). We also found that TAX-4 was mislocalized to the

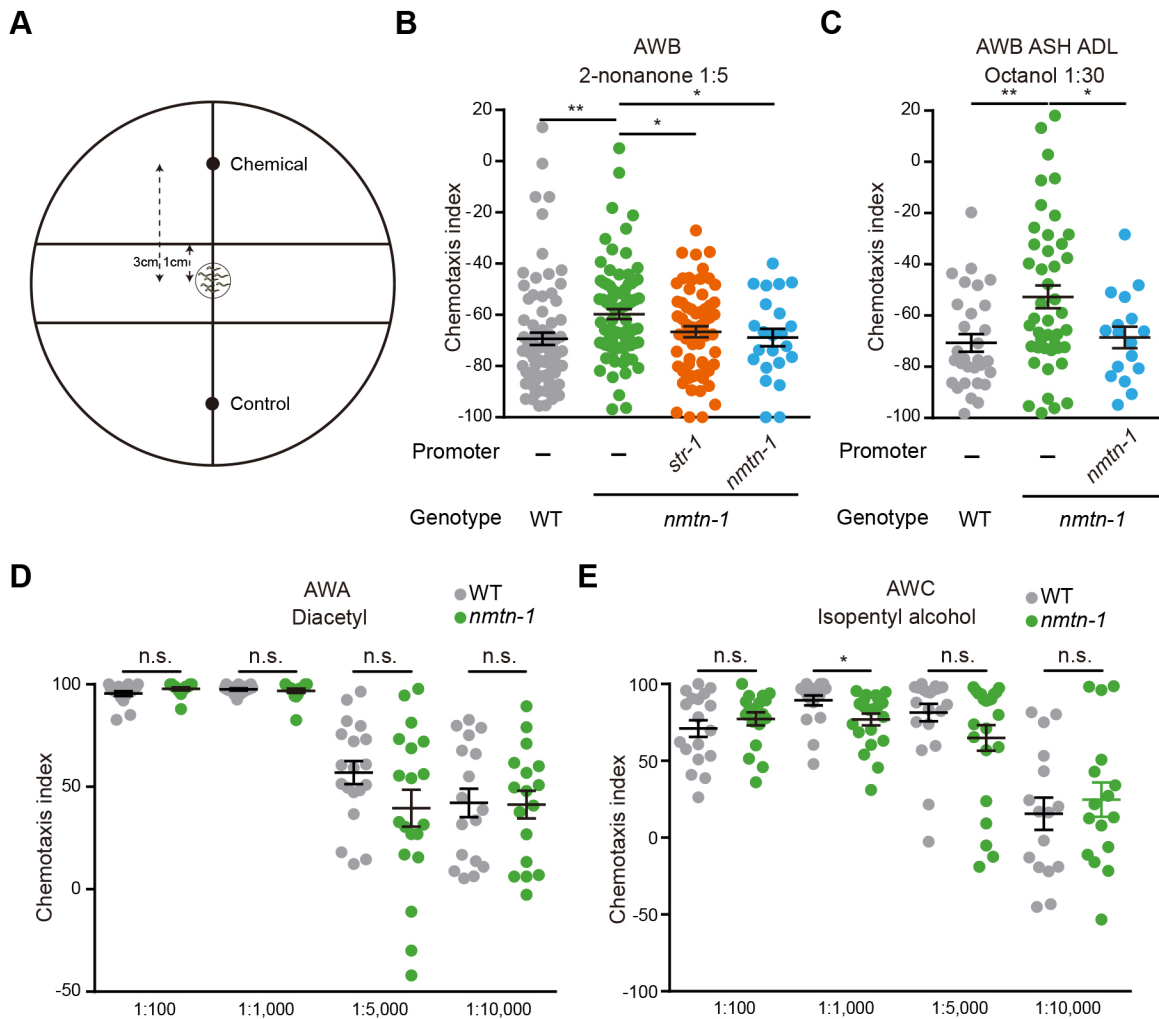


Fig. 3. *nmtn-1* mutants have defects in AWB-mediated aversion behaviors. (A) Schematic illustration of the chemotaxis assays. (B) Quantification of chemotaxis indexes for AWB-mediated aversion behaviors to 2-nonanone in WT and *nmtn-1* mutants. The reduction in behavioral responses to 2-nonanone in *nmtn-1* mutants can be rescued by expression of NMTN-1 under its endogenous promoter or the AWB-specific *str-1* promoter. $n=79$ for WT, $n=85$ for *nmtn-1* mutants, $n=64$ for *Pstr-1* rescue, and $n=23$ for *Pnmtn-1* rescue. (C) Quantification of chemotaxis indexes for aversion behaviors to octanol mediated by the AWB, ASH, and ADL neurons in WT and *nmtn-1* mutants. The reduction in behavioral responses to octanol in *nmtn-1* mutants can be rescued by expression of NMTN-1 under its endogenous promoter. $n=30$ for WT, $n=44$ for *nmtn-1* mutants, and $n=17$ for *Pnmtn-1* rescue. (D) Quantification of chemotaxis indexes for AWA-mediated attraction behaviors to diacetyl at the indicated concentrations in WT and *nmtn-1* mutants. $n=17$ for WT and $n=16$ for *nmtn-1* mutants in 1:100 dilution. $n=15$ for WT and $n=16$ for *nmtn-1* mutants in 1:1000 dilution. $n=19$ for WT and $n=19$ for *nmtn-1* mutants in 1:5000 dilution. $n=17$ for WT and $n=17$ for *nmtn-1* mutants in 1:10,000 dilution. (E) Quantification of chemotaxis indexes for AWC-mediated attraction behaviors to isopentyl alcohol at the indicated concentrations in WT and *nmtn-1* mutants. Each dot represents a single population assay calculated as shown. $n=18$ for WT and $n=18$ for *nmtn-1* mutants in 1:100 dilution. $n=19$ for WT and $n=21$ for *nmtn-1* mutants in 1:1000 dilution. $n=22$ for WT and $n=22$ for *nmtn-1* mutants in 1:5000 dilution. $n=16$ for WT and $n=16$ for *nmtn-1* mutants in 1:10,000 dilution. Data are presented as mean \pm s.e.m. * $P < 0.05$; ** $P < 0.01$; n.s., not significant (unpaired two-tailed Student's *t*-test).

TZ region above the BB (SFig. S5B–D). These results suggest that *nmtn-1* mutation might alter IFT cargo localization, and support the conclusion that NMTN-1 is required for the IFT particle movement and cargo transportation in order to support ciliogenesis and the ciliary structure in the AWB neurons.

DISCUSSION

In this study, we revealed how NMTN-1, the *C. elegans* homolog of WDR47, supports AWB cell-specific ciliogenesis and chemosensation in *C. elegans*. We showed that NMTN-1 is expressed in the AWB chemosensory neurons and is enriched in the BB of the AWB cilia. NMTN-1 functions in the AWB neurons to maintain AWB cilia morphology, structural integrity and AWB-mediated aversion behaviors. We further demonstrated that NMTN-1

ensures proper IFT particle movement and cargo delivery in the AWB neurons, promoting ciliogenesis.

WDR47 is a microtubule-associated protein and has been shown to interact with the CAMSAP family proteins for microtubule-mediated processes (Buijs et al., 2021; Chen et al., 2020; Liu et al., 2021). In non-centrosomal microtubules, WDR47 protects CAMSAP2 against katanin-mediated severing and is required for axonal and dendritic development (Buijs et al., 2021). In mammalian multicilia, WDR47 co-operates with CAMSAP family proteins and the microtubule-severing enzyme katanin to generate ciliary central microtubules (Liu et al., 2021). WDR47 also functions through CAMSAP3 to control neuronal migration and the early stages of neuronal polarization, which is important for neonatal mouse survival (Chen et al., 2020). In addition, WDR47

Table 2. Anterograde IFT velocities of middle segments in WT and *nmtn-1* mutants

IFT protein	Strain	Mean velocity ($\mu\text{m/s}$)	n/N	t test	Bonferroni correction
AWB					
<i>Pstr-1::KAP-1::mNG</i>	WT	0.640 \pm 0.01	81/5		
<i>Pstr-1::KAP-1::mNG</i>	<i>nmtn-1</i>	0.644 \pm 0.01	153/7	n.s.	n.s.
<i>Pstr-1::OSM-3::mNG</i>	WT	0.865 \pm 0.02	104/7		
<i>Pstr-1::OSM-3::mNG</i>	<i>nmtn-1</i>	0.944 \pm 0.01	160/4	***	***
<i>Pstr-1::OSM-6::mNG</i>	WT	0.628 \pm 0.02	70/5		
<i>Pstr-1::OSM-6::mNG</i>	<i>nmtn-1</i>	0.529 \pm 0.01	80/7	***	**
<i>Pstr-1::OSM-6::mNG</i>	<i>kap-1;nmtn-1</i>	1.091\pm0.04	83/6	****	****
<i>Pstr-1::OSM-6::mNG</i>	<i>klp-11;nmtn-1</i>	1.006\pm0.03	70/5	****	****
<i>Pstr-1::OSM-6::mNG</i>	<i>osm-3;nmtn-1</i>	0.551\pm0.01	72/3	n.s.	n.s.
<i>Pstr-1::OSM-6::mNG</i>	<i>bbs-8;nmtn-1</i>	0.695\pm0.01	72/4	****	***
ASH/ADL					
<i>Pstrb-6::OSM-6::mNG</i>	WT	0.809 \pm 0.01	180/8		
<i>Pstrb-6::OSM-6::mNG</i>	<i>nmtn-1</i>	0.834 \pm 0.01	175/6	n.s.	n.s.

* $P < 0.05$; *** $P < 0.001$; **** $P < 0.0001$; n.s. not significant. *t*-tests were unpaired and two-tailed. Values given in bold are where statistical analyses were performed against *nmtn-1* mutants rather than WT animals.

has been shown to interact with microtubule-associated protein 8 (Wang et al., 2012) and participates in several microtubule-mediated processes including neural stem cell proliferation, radial migration, and growth cone dynamics (Kannan et al., 2017). Thus, multiple studies have conceptually linked WDR47 with the regulation of microtubule-associated processes in neuron axons, dendrites and motile cilia. In the present study, we discovered an additional role of NMTN-1 in IFT particle movement and cell-specific ciliogenesis. It is likely that NMTN-1 and particularly the mammalian homolog WDR47 control IFT particle movement via regulating ciliary microtubule networks.

Our results illustrate a cell-specific function of NMTN-1 in ciliogenesis. This cell-specific modulation might have evolved to accommodate different olfactory receptors, channels and/or IFT machinery in other chemosensory neurons to support diversified functions (Mukhopadhyay et al., 2007; Silverman and Leroux, 2009; Wojtyniak et al., 2013). Note that previous studies have reported that IFT-A molecules differentially regulate sensory cilia structures. IFT-121 and IFT-140 are required for all examined cilia in the amphid and phasmid neurons, whereas IFT-139 is required for ciliogenesis of AWC neuron-specific cilia (Scheidel and Blacque, 2018). KLP-6, a conserved member of kinesin-3 family, regulates IFT in the male-specific cilia (Morsci and Barr, 2011). In addition, a few endocytic genes regulate ciliary and periciliary membrane compartment morphology in different cilia types, including the AWB cilia and three channel cilia (Kaplan et al., 2012). Similar to chemosensory neurons in *C. elegans*, mammalian olfactory sensory neurons are also divided into discrete subpopulations that contain distinct subfamilies of olfactory receptors in the cilia (Bear et al., 2016). It will be quite interesting to explore the possibility that WDR47 orthologs might regulate the primary cilia of olfactory sensory neurons in mammals in a cell-specific manner.

Many WDR proteins, such as CHE-2, IFTA-1, DAF-10, CHE-11 and OSM-1 [homologs of mammalian IFT80, WDR35 (also known as IFT121), IFT122, IFT140 and IFT172, respectively] are also required for ciliogenesis in analogy to WDR47/NMTN-1 (Fujiwara et al., 1999; Qin et al., 2001; Quidwai et al., 2021). They are all mobile and act as IFT-binding proteins. However, NMTN-1 does not undergo IFT, so we speculate that NMTN-1 might indirectly regulate IFT machinery. How does NMTN-1 regulate the IFT velocities? Our observation that *nmtn-1* perturbs the velocity distributions of IFT components has also been reported in *nphp-4* and *arl-13* mutants (Cevik et al., 2010; Jauregui et al., 2008). The velocity of OSM-3 is increased, whereas the

velocity of OSM-6 is decreased in *nphp-4* and *arl-13* mutants. On the other hand, the velocity of KAP-1 is unchanged and decreased in *nphp-4* and *arl-13* mutants, respectively. These studies also showed that OSM-6 is associated with a kinesin-II other than OSM-3 in the absence of *nphp-4* (Jauregui et al., 2008) and that OSM-3 is uncoupled from kinesin-II in *arl-13* mutants (Cevik et al., 2010). In WT animals, the kinesin-II and OSM-3 units are linked by the BBS proteins, and, among these, BBS-7 and BBS-8 are required to stabilize kinesin-II and OSM-3 (Ou et al., 2005; Pan et al., 2006). In addition, a conserved ciliary protein, DYF-1, is specifically required for OSM-3 to dock onto and move IFT particles (Ou et al., 2005). We suspect that NMTN-1 might interact with BBS-7, BBS-8 and/or DYF-1 to maintain the coupling of OSM-3 and kinesin-II, or to regulate the binding of IFT particles with motor proteins. The overall effects lead to reduction of cargoes transported to the cilia. This hypothesis is consistent with the observation that IFT cargo TAX-4 was detained in the base of the AWB cilia in some *nmtn-1* mutants.

MATERIALS AND METHODS

Animals

C. elegans were maintained under standard conditions at 20°C on nematode growth medium (NGM; Stiernagle, 2006) plates seeded with *Escherichia coli* OP50. All *C. elegans* strains were derived from the WT Bristol N2 (*Caenorhabditis* Genetics Center) strain. The *nmtn-1* mutant has a 483 bp deletion in the second exon (chr1: 29916/29917-30399/30400). Transgenic animals were prepared by microinjection, and integrated transgenes were isolated following UV irradiation. A complete list of strains is provided in Table S1.

Plasmids

All expression vectors used are pPD49.26 or pPD95.75 (Dr Andrew Fire's laboratory, Stanford, CA, USA). A 3 kb *str-2* promoter was amplified from genomic DNA and cloned for expression in AWC chemosensory neurons. A 3 kb *odr-10* promoter was amplified from genomic DNA and cloned for expression in AWA chemosensory neurons. A 3 kb *str-1* promoter was amplified from genomic DNA and cloned for expression in AWB chemosensory neurons. A 3 kb *srb-6* promoter was amplified from genomic DNA and cloned for expression in ADF, ADL and ASH chemosensory neurons. A complete list of primers used for cloning is provided in Table S1.

Live imaging and analysis

All hermaphrodites imaged were young adult animals. Worms were anesthetized with 30 $\mu\text{g}/\mu\text{l}$ 2,3-butanedione monoxime (Sigma). The 2% agarose liquid was dropped onto the microscope slide and kept at 95°C in the

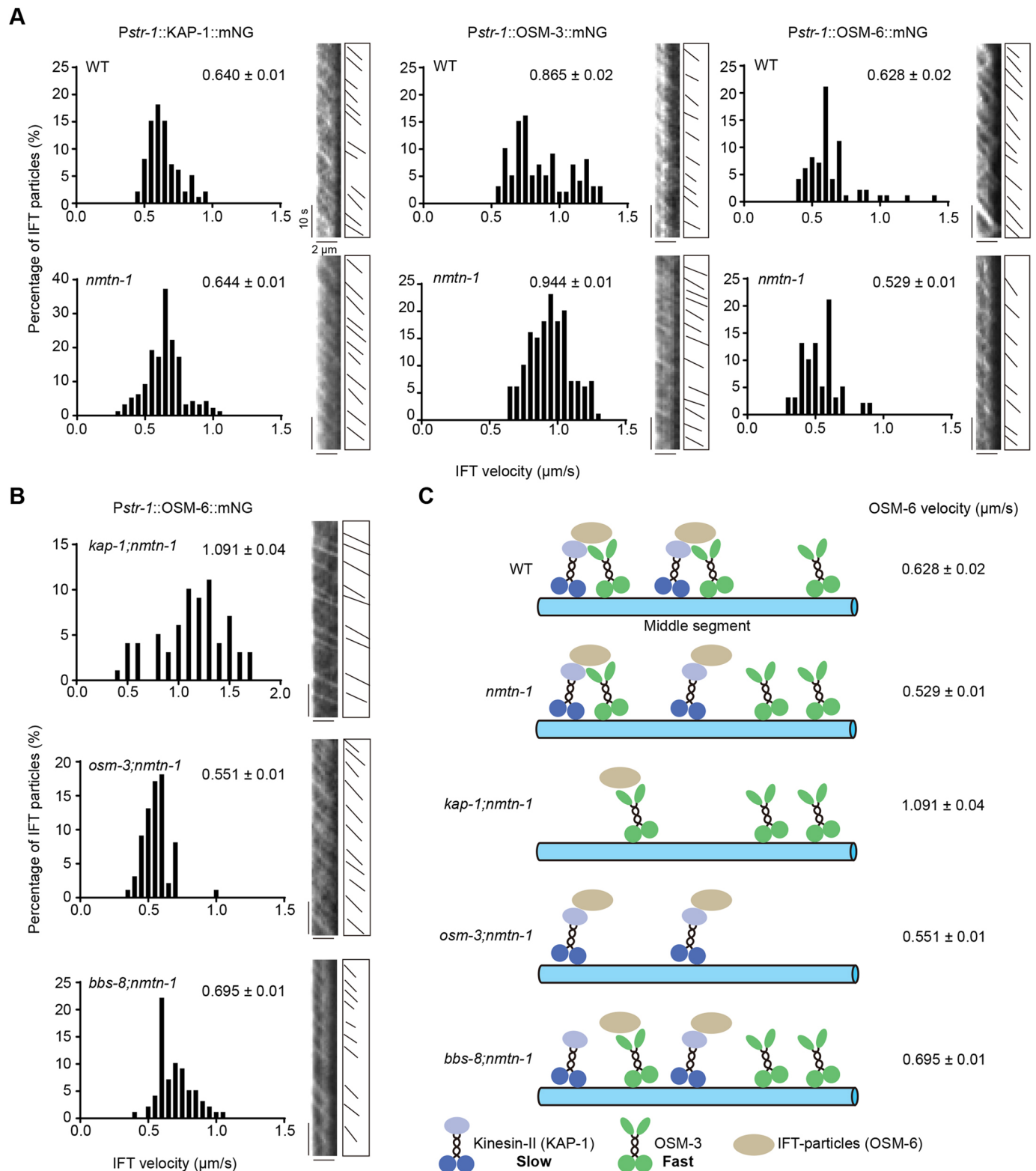


Fig. 4. IFT velocities are altered in *nmtn-1* mutants. (A) Histograms and kymographs of KAP-1::mNG, OSM-3::mNG, and OSM-6::mNG anterograde middle segment velocities in the AWB cilia of WT and *nmtn-1* mutants. KAP-1::mNG, OSM-3::mNG and OSM-6::mNG were expressed under the AWB-specific *str-1* promoter. (B) Histograms and kymographs of OSM-6::mNG anterograde middle segment velocities in the AWB cilia of *kap-1;nmtn-1* mutants, *osm-3;nmtn-1* mutants and *bbs-8;nmtn-1* mutants. In A and B, average velocities are indicated at the top right in each panel as mean \pm s.e.m. A schematic of the traces on the kymograph is provided to the right of the main kymograph images. Scale bars: 2 μm (horizontal), 10 s (vertical). (C) Cartoon illustration showing anterograde IFT in the middle segment of the AWB cilia in WT and mutant animals.

water bath. Then the second slide was placed over the agarose to create a smooth and thin layer. After the agarose had solidified, the slides were slowly separated from each other. Fluorescence images were collected on a fluorescence microscope with a 100× (NA=1.4) objective on an Olympus microscope (BX53) and a Nikon spinning disc confocal microscope (Yokogawa CSU-W1) equipped with a 60× oil objective. The images were further processed using ImageJ software, and the colocalization was assessed with the Channel Tool function.

For the time-lapse imaging experiment, young adult animals were immobilized with 10 mM levamisole in M9 buffer on 5% agarose pads. The images were taken on a Nikon spinning disc confocal microscope (Yokogawa CSU-W1) with a 60× oil objective. The exposure time of the time-lapse images was 300 ms over a 1 min total imaging time. We used ImageJ software to process images, generate kymographs and quantify IFT velocity. To ensure the quality of images used for quantification, only movies with worms in stable focal planes were used to generate kymographs. The anterograde kymographs were generated with the Reslice function in ImageJ by manually drawing lines along the AWB cilia. The velocities were calculated using the formula: $\text{velocity} = \text{ABS}(\text{COT}(\text{RADIANS}(\text{Angle}))) * 0.18 / 0.3$ where 'Angle' is the angle of the oblique line in kymographs, 0.18 is the pixel resolution, and 0.3 is exposure time (300 ms).

Dye-filling assay

Worms were washed with M9 buffer, and then incubated with the fluorescent lipophilic carbocyanine dye Dil (Molecular Probes) in the dark for 30 min at room temperature. Dil was prepared as a 1 mg/ml stock solution in DMSO and diluted at 1:100 in M9 buffer. After incubation with Dil, worms were washed with M9 buffer again and transferred to seeded NGM plates for 1 or 2 h to remove autofluorescence from the gut. Worms were then anesthetized with 10% levamisole, mounted on the 2% agar pads and imaged using a Nikon spinning disc confocal microscope (Yokogawa CSU-W1) with a 60× oil objective.

Chemotaxis assay

The plates used for the chemotaxis assay are 9 cm tissue culture dishes containing 10 ml of 1.6% agar, 5 mM potassium phosphate (pH 6.0), 1 mM CaCl_2 and 1 mM MgSO_4 . The plates were autoclaved and stocked at 4°C. On the day of the experiments, the plates were taken out from 4°C to sit at room temperature until they were dry. The middle of the plates was marked on the back as the site for the initial location of the animals. In addition, two marks were labeled ~3 cm away from the middle of the plate. The two marks represent the sites for chemical and ethanol (control).

Synchronized young adult animals were washed three times with 1 ml S Basal buffer [5.9 g NaCl, 50 ml 1 M potassium phosphate (pH 6.0), 1 ml cholesterol (5 mg/ml in ethanol) in 1 l ddH_2O]. Then the worms were washed two times with 1 ml water to remove bacteria, and were centrifuged at 1000 g for 2 mins. The supernatants were removed as much as possible. 5 µl solution containing the worms was pipetted in the center of the plates. 1 µl of 1 M sodium azide was added to freeze animals on the control and chemical side. Next, 1 µl ethanol was added on the control side, and 1 µl chemical was added on the chemical side. After 2 h, the number of animals on both the control and chemical side were counted. Note that worms within 1 cm from the center were excluded. The chemotaxis indexes were calculated by using this formula: $(\text{Number of animals on the chemical side} - \text{Number of animals on control side}) / (\text{Number of animals on chemical side} + \text{Number of animals on the control side})$. The chemicals use are detailed in Table S1.

Scanning electron microscopy

We used a type A carrier (100 µm+200 µm, Leica, #16770181), dipped it to the 200 µm surface with 1-hexadecene, and dried it with filter paper. The young adult hermaphrodites treated with 10 mM levamisole were transferred to M9 buffer (Stiernagle, 2006) containing 10% bovine serum albumin in the cavity of the carrier. The flat surface of the type B carrier (0+300 µm, Leica, #16770182) was placed on top to enclose the worms in the cavity of the aluminum planchette. The specimen–planchette sandwich was rapidly frozen using a Leica EM ICE high-pressure freezing system.

Freeze-substitution was performed at low temperature (−90°C) over 3 days in a solution containing 2% osmium tetroxide and 1% uranyl acetate in anhydrous acetone using a Leica EM AFS2 freeze-substitution system. The temperature was progressively increased up to 4°C. Samples were washed four times with anhydrous acetone (10 min each), and then successively infiltrated with a mixture of acetone resin of 3:1; 1:1; 1:3, respectively. Then samples were infiltrated and embedded in resin at room temperature and polymerized in an oven at 60°C for three days. Resin blocks with specimens were trimmed so that the block face was perpendicular to the longitudinal axis of the worm nose for sections, while keeping a small amount of resin around the specimen. Ultrathin sections (70 nm thickness) were collected and post-stained with 1% uranyl acetate for 15 min and 0.08 M lead citrate for another 10 min. Sections were imaged on a GeminiSEM460 scanning electron microscope (Zeiss).

Quantification and statistical analysis

All plots were generated by GraphPad Prism (version 7.0a). All scatterplots are shown as mean±s.e.m. We used unpaired two-tailed Student's *t*-test and Bonferroni correction to determine statistical differences except for the Chi-square test in Fig. 2B.

Acknowledgements

We want to thank Xiumin Yan and Yidong Shen at the Institute of Biochemistry and Cell Biology, Shanghai Institutes for Biological Sciences, Chinese Academy of Sciences for kindly providing *nmt-1* mutants and fluorescent lipophilic carbocyanine dye Dil. We thank Guangshuo Ou at School of Life Sciences, Tsinghua University for kindly providing OSM-6::GFP strain and Qing Wei at Shenzhen Institutes of Advanced Technology, Chinese Academy of Sciences for providing *Par13::MKS-5::mCherry* and *Par13::DYF-19::mCherry* plasmids. We thank the *C. elegans* Genetics Stock Center, National BioResource Project (NBRP) for sharing strains and reagents. We also thank Core Facility of Basic Medical Sciences, Shanghai Jiao Tong University School of Medicine, the Molecular Imaging Core Facility (MICF) at the School of Life Science and Technology, ShanghaiTech University for help in imaging, and Linjie Li at the Bio-EM facility at ShanghaiTech University for technical support on SEM data collection.

Competing interests

The authors declare no competing or financial interests.

Author contributions

Conceptualization: C.-X.S., X.-J.T., Q.L.; Methodology: C.-X.S., X.-T.Z., W.-X.Z., R.L.; Validation: C.-X.S.; Investigation: C.-X.S., X.-T.Z., W.-X.Z.; Data curation: C.-X.S., X.-T.Z., W.-X.Z., R.L.; Writing - original draft: C.-X.S., X.-J.T., Q.L.; Writing - review & editing: C.-X.S., X.-J.T., Q.L.; Visualization: X.-J.T., Q.L.; Supervision: X.-J.T., Q.L.; Project administration: X.-J.T., Q.L.; Funding acquisition: X.-J.T., Q.L.

Funding

This work was supported by the National Natural Science Foundation of China (32122038, 31970933 and 32170963), the National Key Research and Development Program of China (2021ZD0203100 and 2021ZD0202500), the Basic Research Project from the Science and Technology Commission of Shanghai Municipality (21JC1404500, 21ZR1481000, and 19JC1414100), the Shuguang Program supported by Shanghai Education Development Foundation and Shanghai Municipal Education Commission (21SG16), the Program for Young Scholars of Special Appointment at Shanghai Institutions of Higher Learning (QD2018017), and Innovative Research Team of High-Level Local Universities in Shanghai (SHSMU-ZDCX20211102).

Data availability

All relevant data can be found within the article and its supplementary information.

Peer review history

The peer review history is available online at <https://journals.biologists.com/jcs/lookup/doi/10.1242/jcs.260303.reviewer-comments.pdf>

References

- Bargmann, C. I. (2006). Chemosensation in *C. elegans*. In *WormBook* (ed. The *C. elegans* Research Community, WormBook), <http://www.wormbook.org>. doi:10.1895/wormbook.1.123.1
- Bae, Y.-K. and Barr, M. M. (2011). Sensory roles of neuronal cilia: cilia development, morphogenesis, and function in *C. elegans*. *Front. Biosci.* **13**, 5959–5974.

- Bear, D. M., Lassance, J. M., Hoekstra, H. E. and Datta, S. R. (2016). The evolving neural and genetic architecture of vertebrate olfaction. *Curr. Biol.* **26**, R1039-R1049. doi:10.1016/j.cub.2016.09.011
- Berbari, N. F., O'Connor, A. K., Haycraft, C. J. and Yoder, B. K. (2009). The primary cilium as a complex signaling center. *Curr. Biol.* **19**, R526-R535. doi:10.1016/j.cub.2009.05.025
- Bloodgood, R. A. (2010). Sensory reception is an attribute of both primary cilia and motile cilia. *J. Cell Sci.* **123**, 505-509. doi:10.1242/jcs.066308
- Brown, J. M. and Witman, G. B. (2014). Cilia and diseases. *Bioscience* **64**, 1126-1137. doi:10.1093/biosci/biu174
- Brust-Mascher, I., Ou, G. and Scholey, J. M. (2013). Measuring rates of intraflagellar transport along *Caenorhabditis elegans* sensory cilia using fluorescence microscopy. *Methods Enzymol.* **524**, 285-304. doi:10.1016/B978-0-12-397945-2.00016-0
- Buijs, R. R., Hummel, J. J. A., Burute, M., Pan, X., Cao, Y., Stucchi, R., Altelaar, M., Akhmanova, A., Kapitein, L. C. and Hoogenraad, C. C. (2021). WDR47 protects neuronal microtubule minus ends from katanin-mediated severing. *Cell Rep.* **36**, 109371. doi:10.1016/j.celrep.2021.109371
- Cevik, S., Hori, Y., Kaplan, O. I., Kida, K., Toivenon, T., Foley-Fisher, C., Cottell, D., Katada, T., Kontani, K. and Blacque, O. E. (2010). Joubert syndrome ARL13B functions at ciliary membranes and stabilizes protein transport in *Caenorhabditis elegans*. *J. Cell Biol.* **188**, 953-969. doi:10.1083/jcb.200908133
- Challis, R. C., Tian, H., Wang, J., He, J., Jiang, J., Chen, X., Yin, W., Connelly, T., Ma, L., Yu, C. R. et al. (2015). An olfactory cilia pattern in the mammalian nose ensures high sensitivity to odors. *Curr. Biol.* **25**, 2503-2512. doi:10.1016/j.cub.2015.07.065
- Chao, M. Y., Komatsu, H., Fukuto, H. S., Dionne, H. M. and Hart, A. C. (2004). Feeding status and serotonin rapidly and reversibly modulate a *Caenorhabditis elegans* chemosensory circuit. *Proc. Natl. Acad. Sci. USA* **101**, 15512-15517. doi:10.1073/pnas.0403369101
- Chen, Y., Zheng, J., Li, X., Zhu, L., Shao, Z., Yan, X. and Zhu, X. (2020). Wdr47 controls neuronal polarization through the camsap family microtubule minus-end-binding proteins. *Cell Rep.* **31**, 107526. doi:10.1016/j.celrep.2020.107526
- Coburn, C. M. and Bargmann, C. I. (1996). A putative cyclic nucleotide-gated channel. *Neuron* **17**, 695-706. doi:10.1016/S0896-6273(00)80201-9
- Cornelia, I., Bargmann, T. E. H. and Robert Horvitz, H. (1993). Odorant-selective genes and neurons mediate olfaction in *C. elegans*. *Cell* **74**, 515-527.
- Dasgupta, A. and Amack, J. D. (2016). Cilia in vertebrate left-right patterning. *Philos. Trans. R. Soc. Lond. B Biol. Sci.* **371**, 20150410.
- Doroquez, D. B., Berciu, C. and Nicastro, D. (2014). A high-resolution morphological and ultrastructural map of anterior sensory cilia and glia in *Caenorhabditis elegans*. *Elife* **3**, e01948.
- Emily, R., Troemel, B. E. K. and Bargmann, C. I. (1997). Reprogramming chemotaxis responses: sensory neurons define olfactory preferences in *C. elegans*. *Cell* **91**, 161-169. doi:10.1016/S0092-8674(00)80399-2
- Fujiwara, M., Ishihara, T. and Katsura, I. (1999). A novel WD40 protein, CHE-2, acts cell autonomously in the formation of *C. elegans* sensory cilia. *Development* **126**, 4839-4848.
- Goetz, S. C. and Anderson, K. V. (2010). The primary cilium: a signalling centre during vertebrate development. *Nat. Rev. Genet.* **11**, 331-344. doi:10.1038/nrg2774
- Hao, L. and Scholey, J. M. (2009). Intraflagellar transport at a glance. *Cell Sci. Glance* **122**, 889-892.
- Hart, A. C. and Chao, M. Y. (2010). From Odors to Behaviors in *Caenorhabditis elegans*. In *The Neurobiology of Olfaction* (ed Menini A), Chapter 1. Boca Raton (FL): CRC Press/Taylor & Francis.
- Inglis, P. N., Ou, G., Leroux, M. R. and Scholey, J. M. (2007). The sensory cilia of *Caenorhabditis elegans*. In *WormBook* (ed. The C. elegans Research Community), <http://www.wormbook.org>. doi:10.1895/wormbook.1.126.2
- Ishikawa, H. and Marshall, W. F. (2011). Ciliogenesis: building the cell's antenna. *Nat. Rev. Mol. Cell Biol.* **12**, 222-234. doi:10.1038/nrm3085
- Jauregui, A. R., Nguyen, K. C. Q., Hall, D. H. and Barr, M. M. (2008). The *Caenorhabditis elegans* nephrocytins act as global modifiers of cilium structure. *J. Cell Biol.* **180**, 973-988. doi:10.1083/jcb.200707090
- Jenkins, P. M., McEwen, D. P. and Martens, J. R. (2009). Olfactory cilia: linking sensory cilium function and human disease. *Chem. Senses* **34**, 451-464. doi:10.1093/chemse/bjp020
- Jordan, M. A. and Pigino, G. (2021). The structural basis of intraflagellar transport at a glance. *J. Cell Sci.* **134**, jcs247163.
- Jung, I., Powers, T. R. and Valles, J. M. Jr. (2014). Evidence for two extremes of ciliary motor response in a single swimming microorganism. *Biophys. J.* **106**, 106-113. doi:10.1016/j.bpj.2013.11.3703
- Kannan, M., Bayam, E., Wagner, C., Rinaldi, B., Kretz, P. F., Tilly, P., Roos, M., McGilweh, L., Bärf, S., Minocha, S. et al. (2017). WD40-repeat 47, a microtubule-associated protein, is essential for brain development and autophagy. *Proc. Natl. Acad. Sci. USA* **114**, E9308-E9317. doi:10.1073/pnas.1713625114
- Kaplan, O. I., Doroquez, D. B., Cevik, S., Bowie, R. V., Clarke, L., Sanders, A. A., Kida, K., Rappoport, J. Z., Sengupta, P. and Blacque, O. E. (2012). Endocytosis genes facilitate protein and membrane transport in *C. elegans* sensory cilia. *Curr. Biol.* **22**, 451-460.
- Kim, Y. and Kim, S. H. (2020). WD40-repeat proteins in ciliopathies and congenital disorders of endocrine system. *Endocrinol. Metab. (Seoul)* **35**, 494-506. doi:10.3803/EnM.2020.302
- Kobayashi, T. and Dynlacht, B. D. (2011). Regulating the transition from centriole to basal body. *J. Cell Biol.* **193**, 435-444. doi:10.1083/jcb.201101005
- Kulaga, H. M., Leitch, C. C., Eichers, E. R., Badano, J. L., Lesemann, A., Hoskins, B. E., Lupski, J. R., Beales, P. L., Reed, R. R. and Katsanis, N. (2004). Loss of BBS proteins causes anosmia in humans and defects in olfactory cilia structure and function in the mouse. *Nat. Genet.* **36**, 994-998. doi:10.1038/ng1418
- Lechtreck, K. F. (2015). IFT-cargo interactions and protein transport in cilia. *Trends Biochem. Sci.* **40**, 765-778. doi:10.1016/j.tibs.2015.09.003
- Li, Q. and Liberles, S. D. (2015). Aversion and attraction through olfaction. *Curr. Biol.* **25**, R120-R129.
- Liang, Y., Pang, Y., Wu, Q., Hu, Z., Han, X., Xu, Y., Deng, H. and Pan, J. (2014). FLA8/KIF3B phosphorylation regulates kinesin-II interaction with IFT-B to control IFT entry and turnaround. *Dev. Cell* **30**, 585-597. doi:10.1016/j.devcel.2014.07.019
- Liu, H., Zheng, J., Zhu, L., Xie, L., Chen, Y., Zhang, Y., Zhang, W., Yin, Y., Peng, C., Zhou, J. et al. (2021). Wdr47, Camsaps, and Katanin cooperate to generate ciliary central microtubules. *Nat. Commun.* **12**, 5796. doi:10.1038/s41467-021-26058-5
- Ma, M., Stoyanova, M., Rademacher, G., Dutcher, S. K., Brown, A. and Zhang, R. (2019). Structure of the decorated ciliary doublet microtubule. *Cell* **179**, 909-922.e12.
- Marshall, W. F. (2008). Basal bodies: Platforms for Building Cilia. In *Ciliary Function in Mammalian Development* (ed Bradley K. Yoder), pp. 1-22. Academic Press. doi:10.1016/S0070-2153(08)00801-6
- Morsci, N. S. and Barr, M. M. (2011). Kinesin-3 KLP-6 regulates intraflagellar transport in male-specific cilia of *Caenorhabditis elegans*. *Curr. Biol.* **21**, 1239-1244. doi:10.1016/j.cub.2011.06.027
- Mukhopadhyay, S., Lu, Y., Qin, H., Lanjuin, A., Shaham, S. and Sengupta, P. (2007). Distinct IFT mechanisms contribute to the generation of ciliary structural diversity in *C. elegans*. *EMBO J* **26**, 2966-2980. doi:10.1038/sj.emboj.7601717
- Nachury, M. V. (2018). The molecular machines that traffic signaling receptors into and out of cilia. *Curr. Opin. Cell Biol.* **51**, 124-131. doi:10.1016/j.cob.2018.03.004
- Nechipurenko, I. V., Olivier-Mason, A., Kazatskaya, A., Kennedy, J., McLachlan, I. G., Heiman, M. G., Blacque, O. E. and Sengupta, P. (2016). A conserved role for girdin in basal body positioning and ciliogenesis. *Dev. Cell* **38**, 493-506. doi:10.1016/j.devcel.2016.07.013
- O'Hagan, R., Piasecki, B. P., Silva, M., Pirke, P., Nguyen, K. C., Hall, D. H., Swoboda, P. and Barr, M. M. (2011). The tubulin deglutamylase CCEP-1 regulates the function and stability of sensory cilia in *C. elegans*. *Curr. Biol.* **21**, 1685-1694. doi:10.1016/j.cub.2011.08.049
- Olivier-Mason, A., Wojtyniak, M., Bowie, R. V., Nechipurenko, I. V., Blacque, O. E. and Sengupta, P. (2013). Transmembrane protein OSTA-1 shapes sensory cilia morphology via regulation of intracellular membrane trafficking in *C. elegans*. *Development* **140**, 1560-1572.
- Ou, G., Blacque, O. E., Snow, J. J., Leroux, M. R. and Scholey, J. M. (2005). Functional coordination of intraflagellar transport motors. *Nature* **436**, 583-587. doi:10.1038/nature03818
- Ou, G., Koga, M., Blacque, O. E., Murayama, T., Ohshima, Y., Schafer, J. C., Li, C., Yoder, B. K., Leroux, M. R. and Scholey, J. M. (2007). Sensory ciliogenesis in *Caenorhabditis elegans*: assignment of IFT components into distinct modules based on transport and phenotypic profiles. *Mol. Biol. Cell* **18**, 1554-1569. doi:10.1091/mbc.e06-09-0805
- Pan, J., Wang, Q. and Snell, W. J. (2005). Cilium-generated signaling and cilia-related disorders. *Lab. Invest.* **85**, 452-463. doi:10.1038/labinvest.3700253
- Pan, X., Ou, G., Civelekoglu-Scholey, G., Blacque, O. E., Endres, N. F., Tao, L., Mogilner, A., Leroux, M. R., Vale, R. D. and Scholey, J. M. (2006). Mechanism of transport of IFT particles in *C. elegans* cilia by the concerted action of kinesin-II and OSM-3 motors. *J. Cell Biol.* **174**, 1035-1045.
- Pedersen, L. B., Schroder, J. M., Satir, P. and Christensen, S. T. (2012). The ciliary cytoskeleton. *Compr Physiol* **2**, 779-803. doi:10.1002/cphy.c110043
- Prevo, B., Scholey, J. M. and Peterman, E. J. G. (2017). Intraflagellar transport: mechanisms of motor action, cooperation, and cargo delivery. *FEBS J.* **284**, 2905-2931. doi:10.1111/febs.14068
- Qian, K. Y., Zeng, W. X., Hao, Y., Zeng, X. T., Liu, H., Li, L., Chen, L., Tian, F. M., Chang, C., Hall, Q. et al. (2021). Male pheromones modulate synaptic transmission at the *C. elegans* neuromuscular junction in a sexually dimorphic manner. *Elife* **10**, e67170.
- Qin, H. M., Rosenbaum, J. L. and Barr, M. M. (2001). An autosomal recessive polycystic kidney disease gene homolog is involved in intraflagellar transport in *C. elegans* ciliated sensory neurons. *Curr. Biol.* **11**, 457-461. doi:10.1016/S0960-9822(01)00122-1
- Quidwai, T., Wang, J., Hall, E. A., Petriman, N. A., Leng, W., Kiesel, P., Wells, J. N., Murphy, L. C., Keighren, M. A., Marsh, J. A. et al. (2021). A

- WDR35-dependent coat protein complex transports ciliary membrane cargo vesicles to cilia. *elife* **10**, e69786.
- Reiter, J. F. and Leroux, M. R. (2017). Genes and molecular pathways underpinning ciliopathies. *Nat. Rev. Mol. Cell Biol.* **18**, 533–547. doi:10.1038/nrm.2017.60
- Reiter, J. F., Blacque, O. E. and Leroux, M. R. (2012). The base of the cilium: roles for transition fibres and the transition zone in ciliary formation, maintenance and compartmentalization. *EMBO Rep.* **13**, 608–618. doi:10.1038/embor.2012.73
- Ringers, C., Olstad, E. W. and Jurisch-Yaksi, N. (2020). The role of motile cilia in the development and physiology of the nervous system. *Philos. Trans. R. Soc. Lond. B Biol. Sci.* **375**, 20190156. doi:10.1098/rstb.2019.0156
- Scheidel, N. and Blacque, O. E. (2018). Intraflagellar transport complex a genes differentially regulate cilium formation and transition zone gating. *Curr. Biol.* **28**, 3279–3287.e2. doi:10.1016/j.cub.2018.08.017
- Scholey, J. M. (2008). Intraflagellar transport motors in cilia: moving along the cell's antenna. *J. Cell Biol.* **180**, 23–29. doi:10.1083/jcb.200709133
- Schouteden, C., Serwas, D., Palfy, M. and Dammermann, A. (2015). The ciliary transition zone functions in cell adhesion but is dispensable for axoneme assembly in *C. elegans*. *J. Cell Biol.* **210**, 35–44. doi:10.1083/jcb.201501013
- Sengupta, P. (2007). Generation and modulation of chemosensory behaviors in *C. elegans*. *Pflugers Arch.* **454**, 721–734. doi:10.1007/s00424-006-0196-9
- Serwas, D. and Dammermann, A. (2015). Ultrastructural analysis of *Caenorhabditis elegans* cilia. *Methods Cell Biol.* **129**, 341–367. doi:10.1016/bs.mcb.2015.03.014
- Shao, L., El-Jouni, W., Kong, F., Ramesh, J., Kumar, R. S., Shen, X., Ren, J., Devendra, S., Dorschel, A., Wu, M. et al. (2020). Genetic reduction of cilium length by targeting intraflagellar transport 88 protein impedes kidney and liver cyst formation in mouse models of autosomal polycystic kidney disease. *Kidney Int.* **98**, 1225–1241. doi:10.1016/j.kint.2020.05.049
- Sharma, N., Berbari, N. F. and Yoder, B. K. (2008). Ciliary dysfunction in developmental abnormalities and diseases. *Curr. Top. Dev. Biol.* **85**, 371–427. doi:10.1016/S0070-2153(08)00813-2
- Silva, M., Morsci, N., Nguyen, K. C. Q., Rizvi, A., Rongo, C., Hall, D. H. and Barr, M. M. (2017). Cell-specific alpha-tubulin isotype regulates ciliary microtubule ultrastructure, intraflagellar transport, and extracellular vesicle biology. *Curr. Biol.* **27**, 968–980. doi:10.1016/j.cub.2017.02.039
- Silverman, M. A. and Leroux, M. R. (2009). Intraflagellar transport and the generation of dynamic, structurally and functionally diverse cilia. *Trends Cell Biol.* **19**, 306–316. doi:10.1016/j.tcb.2009.04.002
- Soares, H., Carmona, B., Nolasco, S. and Viseu Melo, L. (2019). Polarity in ciliate models: from cilia to cell architecture. *Front. Cell Dev. Biol.* **7**, 240. doi:10.3389/fcell.2019.00240
- Stiernagle, T. (2006) Maintenance of *C. elegans*. In *WormBook* (ed. The *C. elegans* Research Community, WormBook), <http://www.wormbook.org>. doi:10.1895/wormbook.1.101.1
- Taylor, S. R., Santpere, G., Weinreb, A., Barrett, A., Reilly, M. B., Xu, C., Varol, E., Oikonomou, P., Glenwinkel, L., McWhirter, R. et al. (2021). Molecular topography of an entire nervous system. *Cell* **184**, 4329–4347.e23. doi:10.1016/j.cell.2021.06.023
- Tong, Y.-G. and Burglin, T. R. (2010). Conditions for dye-filling of sensory neurons in *Caenorhabditis elegans*. *J. Neurosci. Methods* **188**, 58–61. doi:10.1016/j.jneumeth.2010.02.003
- Uytingco, C. R., Green, W. W. and Martens, J. R. (2019a). Olfactory loss and dysfunction in ciliopathies: molecular mechanisms and potential therapies. *Curr. Med. Chem.* **26**, 3103–3119. doi:10.2174/0929867325666180105102447
- Uytingco, C. R., Williams, C. L., Xie, C., Shively, D. T., Green, W. W., Ukhonov, K., Zhang, L., Nishimura, D. Y., Sheffield, V. C. and Martens, J. R. (2019b). BBS4 is required for intraflagellar transport coordination and basal body number in mammalian olfactory cilia. *J. Cell Sci.* **132**, jcs222331.
- Wang, W., Lundin, V. F., Millan, I., Zeng, A., Chen, X., Yang, J., Allen, E., Chen, N., Bach, G., Hsu, A. et al. (2012). Nemitin, a novel Map8/Map1s interacting protein with Wd40 repeats. *PLoS One* **7**, e33094. doi:10.1371/journal.pone.0033094
- Wei, Q., Xu, Q., Zhang, Y., Li, Y., Zhang, Q., Hu, Z., Harris, P. C., Torres, V. E., Ling, K. and Hu, J. (2013). Transition fibre protein FBF1 is required for the ciliary entry of assembled intraflagellar transport complexes. *Nat. Commun.* **4**, 2750. doi:10.1038/ncomms3750
- Wei, Q., Ling, K. and Hu, J. (2015). The essential roles of transition fibers in the context of cilia. *Curr. Opin. Cell Biol.* **35**, 98–105. doi:10.1016/j.ceb.2015.04.015
- Williams, C. L., Li, C., Kida, K., Inglis, P. N., Mohan, S., Semenec, L., Bialas, N. J., Stupay, R. M., Chen, N., Blacque, O. E. et al. (2011). MKS and NPHP modules cooperate to establish basal body/transition zone membrane associations and ciliary gate function during ciliogenesis. *J. Cell Biol.* **192**, 1023–1041. doi:10.1083/jcb.201012116
- Wojtyniak, M., Brear, A. G., O'Halloran, D. M. and Sengupta, P. (2013). Cell- and subunit-specific mechanisms of CNG channel ciliary trafficking and localization in *C. elegans*. *J. Cell Sci.* **126**, 4381–4395. doi:10.1242/jcs.127274
- Yoshida, K., Hirotsu, T., Tagawa, T., Oda, S., Wakabayashi, T., Iino, Y. and Ishihara, T. (2012). Odour concentration-dependent olfactory preference change in *C. elegans*. *Nat. Commun.* **3**, 739. doi:10.1038/ncomms1750

B

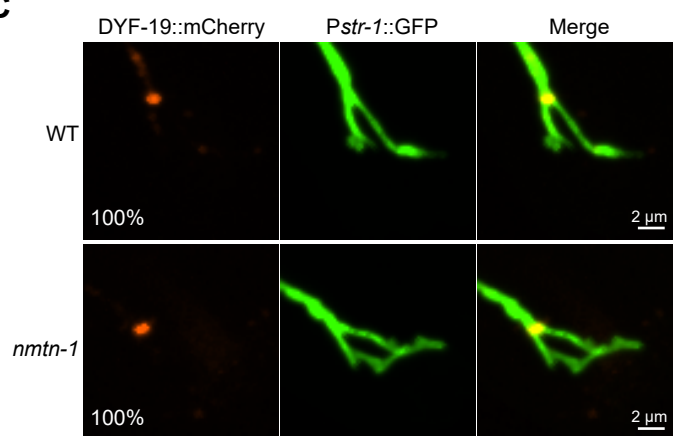


Fig. S1. The expression pattern of *Pnmtn-1::mNG::NMTN-1* at different *C. elegans* developmental stages. (A) Representative images showing *Pnmtn-1::mNG::NMTN-1* signals in the L1, L2, L3, L4, day 1 adult, and day 4 adult of *C. elegans*. The AWB neurons were visualized by expression of *Pstr-1::mCherry*. The dotted lines represent the AWB neurons. White arrowhead, blue arrowhead, and white arrow indicate cilia, the cilia base, and dendrites, respectively. (B) Representative images showing *Pnmtn-1::mNG::NMTN-1* signals in the egg of *C. elegans*. The AWB neurons are marked by expression of *Pstr-1::mCherry*. (C) Representative images of *Pstr-1::DYF-19::mCherry* localization in the AWB neurons of wild type (WT) and *nmtn-1* mutants.

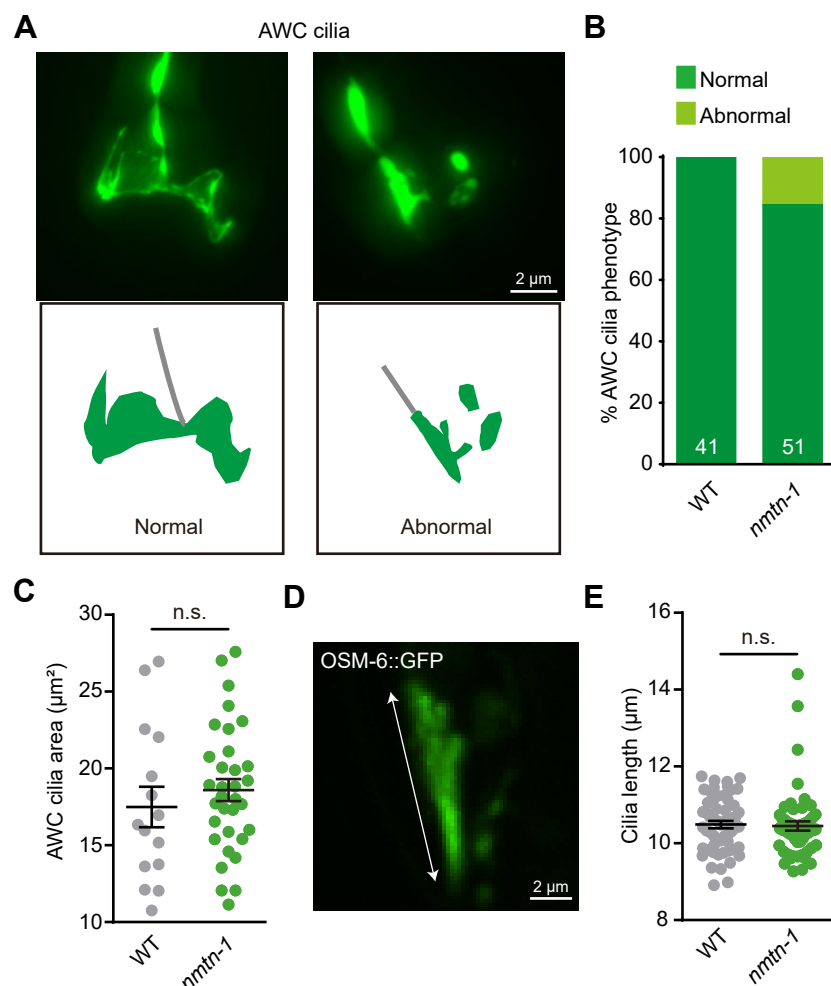


Fig. S2. *nmtn-1* mutants do not have defects in the morphology of other olfactory neurons. (A) Representative images (top) and cartoons (bottom) of the normal and abnormal cilia of the AWC neurons. The AWC cilia were visualized by expression of *Pstr-2::GFP*. (B) The percentages of animals having the normal and abnormal cilia of the AWC neurons in wild type (WT) and *nmtn-1* mutants are shown. (C) Quantification of the AWC cilia area in WT and *nmtn-1* mutants. Each cilium analyzed is represented by a dot. $n = 15$ for WT and $n = 33$ for *nmtn-1* mutants. Data are presented as mean values \pm SEM. (D) Representative image of the OSM-6::GFP fusion protein. The line represents the length of cilia labeled by OSM-6::GFP. (E) Quantification of the cilia length labeled by OSM-6::GFP in WT and *nmtn-1* mutants. Each cilium analyzed is represented by a dot. $n = 57$ for WT and $n = 55$ for *nmtn-1* mutants. Data are presented as mean values \pm SEM. In C and E, n.s. not significant by unpaired two-tailed Student's t-test.

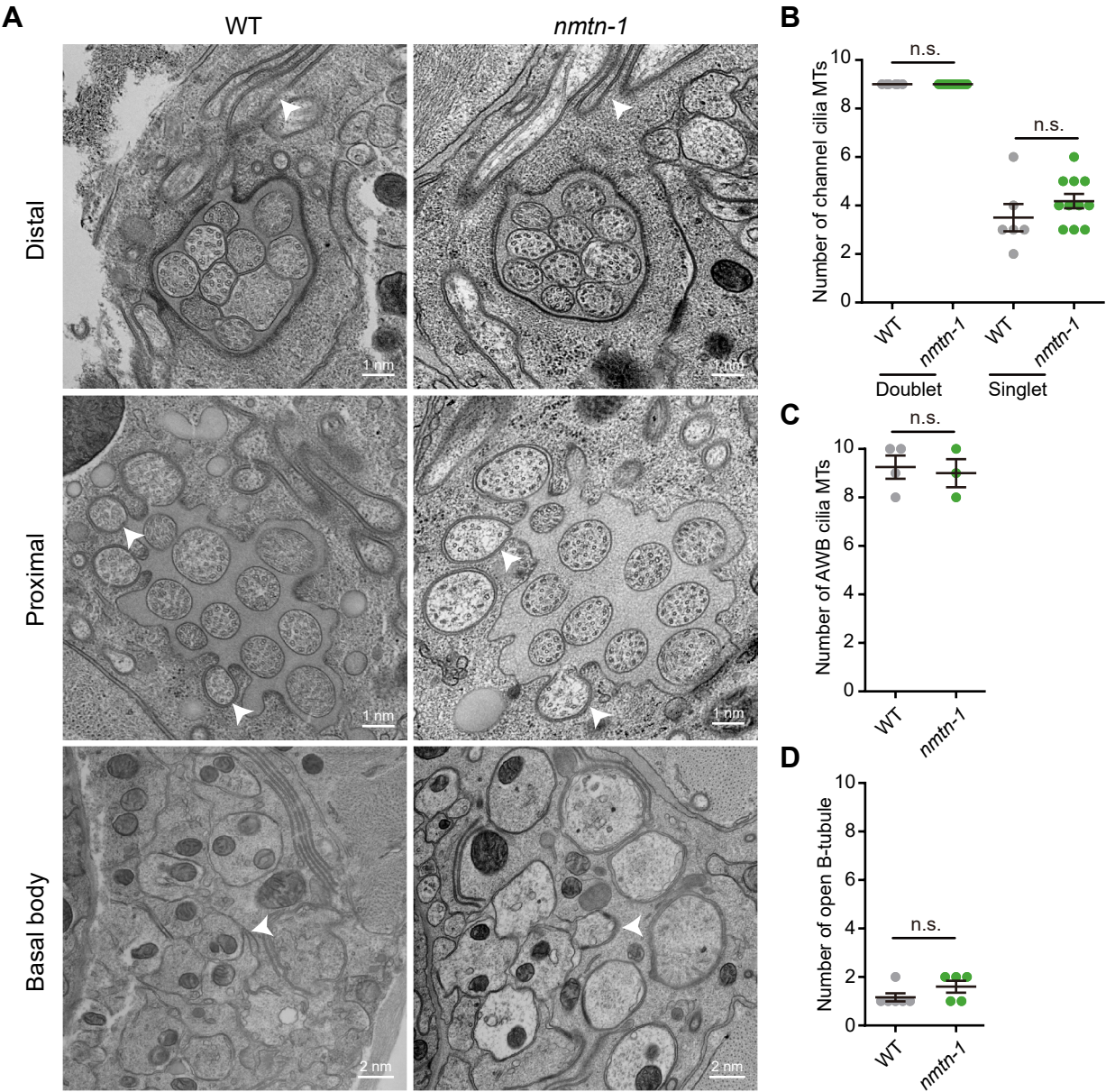


Fig. S3. Ultrastructure of amphid cilia in wild type (WT) and *nmtn-1* mutants.

(A) Representative SEM images (cross-sections) of the amphid cilia at distal, proximal, and basal body in WT and *nmtn-1* mutants. White arrowheads indicate the AWB cilia. (B) Quantification of the channel cilia doublet and singlet microtubules (MTs) in WT and *nmtn-1* mutants. Each cilium analyzed is represented by a dot. $n = 6$ for WT and $n = 11$ for *nmtn-1* mutants. Data are presented as mean values \pm SEM. (C) Quantification of AWB cilia MTs in WT and *nmtn-1* mutants. Each cilium analyzed is represented by a dot. $n = 4$ for WT and $n = 3$ for *nmtn-1* mutants. Data are presented as mean values \pm SEM. (D) Quantification of axonemes having open-B tubules in WT and *nmtn-1* mutants. Each axonemes analyzed is represented by a dot. $n = 6$ for WT and $n = 5$ for *nmtn-1* mutants. Data are presented as mean values \pm SEM. In B, C and D, n.s. not significant by unpaired two-tailed Student's t-test.

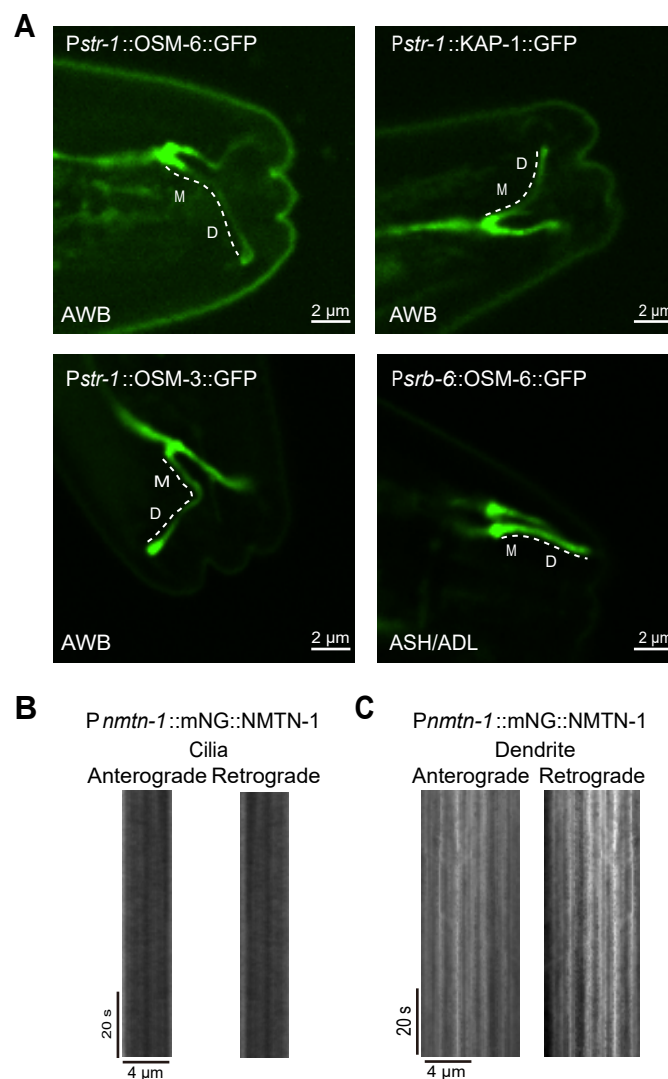


Fig. S4. Representative images of IFT movement in the cilia and dendrites. (A) Representative images of *Pstr-1::OSM-6::GFP*, *Pstr-1::OSM-3::GFP*, *Pstr-1::KAP-1::GFP*, and *Psr-6::OSM-6::GFP* for analyses of IFT particle movement. (B) The kymograph image of NMTN-1 in cilia. The anterograde and retrograde kymograph images of *Pnmtn-1::mNG::NMTN-1* fusion protein show that NMTN-1 is not moving by itself in cilia. (C) The kymograph image of NMTN-1 in the dendrites. The anterograde and retrograde kymograph images of *Pnmtn-1::mNG::NMTN-1* fusion protein show that NMTN-1 is not moving by itself in the dendrites.

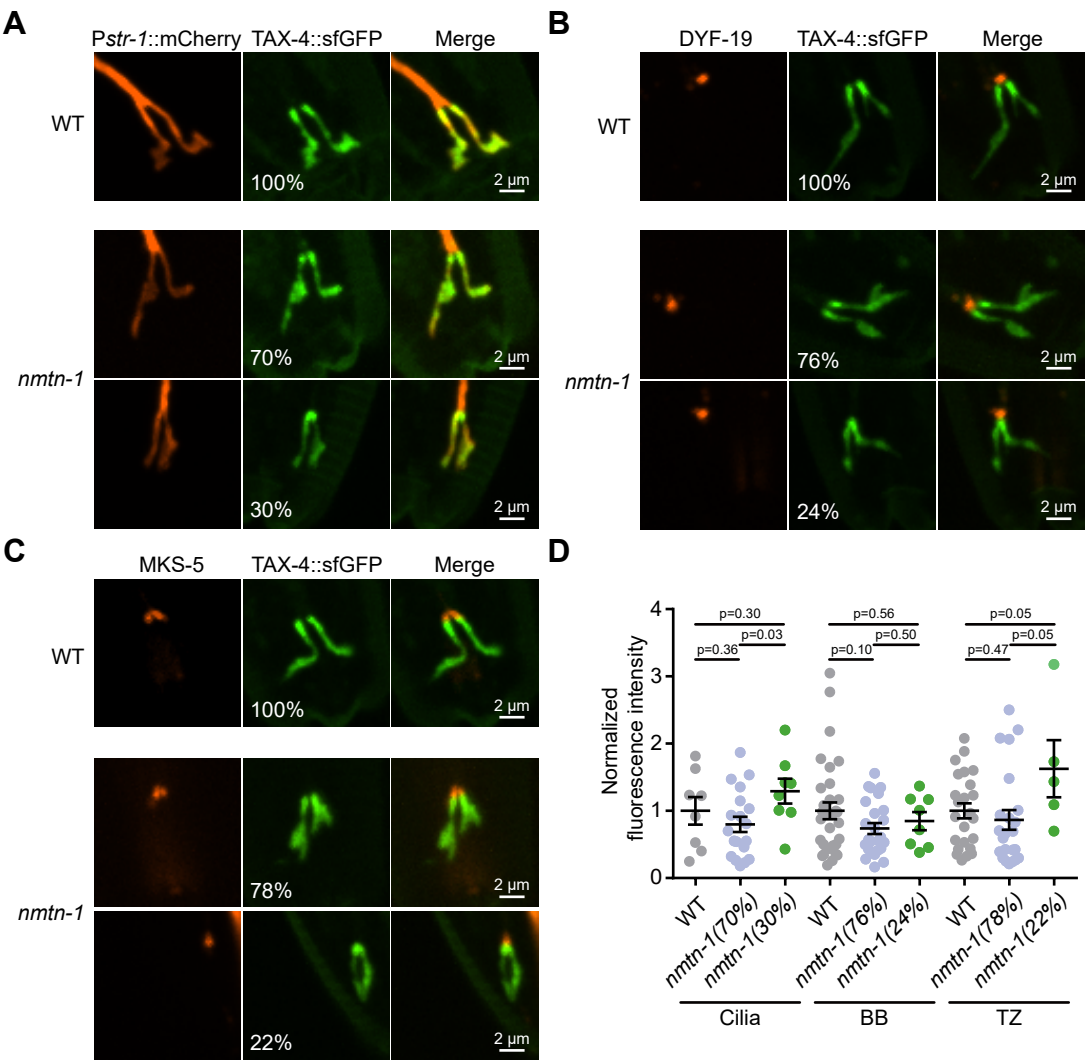


Fig. S5. Localization of ciliary channel may be altered in *nmtn-1* mutants. (A) Representative images of the *Pstr-1::TAX-4::sfGFP* fusion protein and the AWB cilia marked by *Pstr-1::mCherry* in WT and *nmtn-1* mutants. TAX-4 is localized throughout cilia in all of WT animals, while TAX-4 is clearly detained the base of cilia in 30% of *nmtn-1* mutants. (B) Representative images of the *Pstr-1::TAX-4::sfGFP* fusion protein and the BB protein marked by *Pstr-1::DYF-19::mCherry* in WT and *nmtn-1* mutants. TAX-4 is localized throughout cilia in all of WT animals, while TAX-4 is clearly detained the base of cilia in 24% of *nmtn-1* mutants. (C) Representative images of the *Pstr-1::TAX-4::sfGFP* fusion protein and the TZ protein marked by *Pstr-1::MKS-5::mCherry* in WT and *nmtn-1* mutants. TAX-4 is localized throughout cilia in all of WT animals, while TAX-4 is clearly detained the base of cilia in 22% of *nmtn-1* mutants. (D) Quantification of the fluorescence intensities of *Pstr-1::TAX-4::sfGFP* in cilia, BB and TZ of WT and *nmtn-1* mutants. Each cilium analyzed is represented by a dot. n = 8 for WT, n = 19 for 70% *nmtn-1* mutants with normal morphology, n = 8 for 30% *nmtn-1* mutants with abnormal morphology in A. n = 32 for WT, n = 25 for 76% *nmtn-1* mutants with normal morphology, n = 8 for 24% *nmtn-1* mutants with abnormal morphology in B. n = 24 for WT, n = 23 for 78% *nmtn-1* mutants with normal morphology, n = 5 for 22% *nmtn-1* mutants with abnormal morphology in C. Data are presented as mean values \pm SEM. p values were calculated by unpaired two-tailed Student's t-test.

Table S1. List of reagents used in this study

Summary of strain name, genotype, generating method, and resource of *C. elegans* strains. Chemicals, kits, and primers used for generating cell-specific promoters were also listed.

<i>C. elegans</i> strains used in this study			
Strain name	Genotype	Method	Resource
N2	Wild type	-	CGC
TM5438	<i>nmtn-1(tm5438) I</i>	-	NBRP
TXJ0539	<i>xjls0003[Pstr-1::GFP+Pmyo-3::mCherry]</i>	Microinjection	In this study
TXJ0553	<i>nmtn-1(tm5438) I; xjls0003[Pstr-1::GFP+Pmyo-3::mCherry]</i>	Genetic cross	In this study
SYD0202	<i>[OSM-6::GFP]</i>	-	Guangshuo Ou
TXJ0649	<i>nmtn-1(tm5438) I; [OSM-6::GFP]</i>	Genetic cross	In this study
TXJ0230	<i>xjEX0007[Pstr-1::nmtn-1+Pmyo-3::mCherry]</i>	Microinjection	In this study
TXJ0237	<i>xjEX0008[Pstr-1::nmtn-1+Pmyo-3::mCherry]</i>	Microinjection	In this study
TXJ0228	<i>xjEX0009[Pstr-1::nmtn-1+Pmyo-3::mCherry]</i>	Microinjection	In this study
TXJ0235	<i>xjEX0010[Pnmtn-1::nmtn-1+Pmyo-3::mCherry]</i>	Microinjection	In this study
TXJ1649	<i>xjEX0118[Pnmtn-1::nmtn-1+Pmyo-3::mCherry]</i>	Microinjection	In this study
TXJ0486	<i>xjEx0019[Pnmtn-1::mNG::NMTN-1+Pstr-1::mCherry +Plin-44::GFP]</i>	Microinjection	In this study
TXJ1000	<i>xjEx0073[Pnmtn-1::NMTN-1::mNG+Pstr-1::mCherry+Plin-44::GFP]</i>	Microinjection	In this study
TXJ0571	<i>xjEx0031[Pstr-2::GFP+Pmyo-3::mCherry]</i>	Microinjection	In this study
TXJ0570	<i>nmtn-1(tm5438) I; xjEx0031[Pstr-2::GFP+Pmyo-3::mCherry]</i>	Genetic cross	In this study
TXJ0912	<i>xjEx0072[Pstr-1::OSM-6::mNG+Pstr-1::mCherry+Plin-44::GFP]</i>	Microinjection	In this study
TXJ1187	<i>nmtn-1(tm5438) I; xjEx0072[Pstr-1::OSM-6::mNG+Pstr-1::mCherry+Plin-44::GFP]</i>	Genetic cross	In this study
TXJ1614	<i>nmtn-1(tm5438) I; kap-1(ok676) II. xjEx0072[Pstr-1::OSM-6::mNG+Pstr-1::mCherry+Plin-44::GFP]</i>	Genetic cross	In this study

TXJ1615	<i>nmtn-1(tm5438) I; klp-11(tm324)IV. xjEx0072[Pstr-1::OSM-6::mNG+Pstr-1::mCherry+Plin-44::GFP]</i>	Genetic cross	In this study
TXJ1665	<i>nmtn-1(tm5438) I; osm-3(p802) IV. xjEx0072[Pstr-1::OSM-6::mNG+Pstr-1::mCherry+Plin-44::GFP]</i>	Genetic cross	In this study
TXJ1597	<i>nmtn-1(tm5438) I; bbs-8(nx77)V. xjEx0072[Pstr-1::OSM-6::mNG+Pstr-1::mCherry+Plin-44::GFP]</i>	Genetic cross	In this study
TXJ1015	<i>xjEx0074[Pstr-1::TAX-4::sfGFP+ Pstr-1::mCherry+Plin-44::GFP]</i>	Microinjection	In this study
TXJ1206	<i>nmtn-1(tm5438) I; xjEx0074[Pstr-1::TAX-4::sfGFP+ Pstr-1::mCherry+ Plin-44::GFP]</i>	Genetic cross	In this study
TXJ1028	<i>xjEx0075[Pnmtn-1::GFP+Pstr-1::mCherry +Plin-44::GFP]</i>	Microinjection	In this study
TXJ1031	<i>xjEx0076[Pnmtn-1::GFP+Pstr-2::mCherry+Plin-44::GFP]</i>	Microinjection	In this study
TXJ1030	<i>xjEx0077[Pnmtn-1::GFP+Podr-10::mCherry+Plin-44::GFP]</i>	Microinjection	In this study
TXJ1029	<i>xjEx0078[Pnmtn-1::GFP+Psr-6::mCherry+Plin-44::GFP]</i>	Microinjection	In this study
TXJ1229	<i>xjEx0096[Pstr-1::DYF-19::mCherry +Pstr-1::mNG::nmtn-1 +Plin-44::GFP]</i>	Microinjection	In this study
TXJ1669	<i>xjEx0105[Pstr-1::MKS-5::mCherry +Pstr-1::mNG::nmtn-1 +Plin-44::GFP]</i>	Microinjection	In this study
TXJ1311	<i>xjEx0097[Pstr-1::DYF-19::mCherry+ Pstr-1::GFP+Plin-44::GFP]</i>	Microinjection	In this study
TXJ1260	<i>nmtn-1(tm5438) I; xjEx0097[Pstr-1::DYF-19::mCherry+ Pstr-1::GFP+Plin-44::GFP]</i>	Genetic cross	In this study
TXJ1271	<i>xjEx0082[Pnmtn-1::GFP+Pmyo-3::mCherry]</i>	Microinjection	In this study
TXJ1366	<i>xjEx0098[Pstr-1::KAP-1::mNG+Pstr-1::mCherry+Plin-44::GFP]</i>	Microinjection	In this study
TXJ1380	<i>nmtn-1(tm5438) I; xjEx0098[Pstr-1::KAP-1::mNG+Pstr-1::mCherry+Plin-44::GFP]</i>	Genetic cross	In this study
TXJ1399	<i>xjEx0099[Pstr-1::OSM-3::mNG+Pstr-1::mCherry+Plin-44::GFP]</i>	Microinjection	In this study
TXJ1432	<i>nmtn-1(tm5438) I; xjEx0099[Pstr-1::OSM-3::mNG+Pstr-</i>	Genetic cross	In this study

	<i>1::mCherry+Plin-44::GFP]</i>		
TXJ1428	<i>xjEx0100[Psr-6::OSM-6::mNG+Plin-44::GFP]</i>	Microinjection	In this study
TXJ1431	<i>nmtn-1(tm5438) l;</i> <i>xjEx0100[Psr-6::OSM-6::mNG +Plin-44::GFP]</i>	Genetic cross	In this study
TXJ1429	<i>xjEx0101[Pstr-1::TAX-4::sfGFP+ Pstr-1::DYF-19::mCherry+Plin-44::GFP]</i>	Microinjection	In this study
TXJ1430	<i>nmtn-1(tm5438) l;</i> <i>xjEx0101[Pstr-1::TAX-4::sfGFP+ Pstr-1::DYF-19::mCherry + Plin-44::GFP]</i>	Microinjection	In this study
TXJ1660	<i>xjEx0103[Pstr-1::TAX-4::sfGFP+ Pstr-1::MKS-5::mCherry+Plin-44::GFP]</i>	Microinjection	In this study
TXJ1661	<i>nmtn-1(tm5438) l;</i> <i>xjEx0103[Pstr-1::TAX-4::sfGFP+ Pstr-1::MKS-5::mCherry + Plin-44::GFP]</i>	Genetic cross	In this study
TXJ1042	<i>nmtn-1(tm5438) l;</i> <i>xjEx0106[Pstr-1::mNG::NMTN-1 + Plin-44::GFP]</i>	Microinjection	In this study

Key resources table

Key resources table		
Chemicals and kits		
Reagent or Resource	Source	Identifier
2,3-Butanedione monoxime	Sigma	Cat#: B0753
Levamisole hydrochloride	Sigma	Cat#: 31742
Dil	Molecular Probes	Cat#: D-282
2-Nonanone	Aladdin	Cat#: N105585
Diacetyl	Sinopharm	Cat#: 80042427
Octanol	Sangon Biotech	Cat#: A504032-0250
Isopentyl alcohol	Sangon Biotech	Cat#: A610278-0500
QIAprep Spin Miniprep Kit	Qiagen	Cat#: 27106
TIANPrep Rapid Mini Plasmid kit	TIANGEN	Cat#: DP105-03
PrimeSTAR Max DNA Polymerase	Takara	Cat#: R045A
Hieff CLONE™ Plus One Step Cloning Kit	Yeasen	Cat#: 10911ES62
TIANquick Midi Purification Kit	TIANGEN	Cat#: DP204-03

Primers information	
<i>Pstr-1</i> F	aagcttgagtgagaagaatgtcacg
<i>Pstr-1</i> R	gtcgactagtc aaatgatatgaagtt
<i>Pstr-2</i> F	aagcttatataaatcaatgggac
<i>Pstr-2</i> R	gtcgactttatggatcacgagtattc
<i>Podr-10</i> F	aagctttaattttcataattgactc
<i>Podr-10</i> R	gtcgacggagctgtaaggatatctaag
<i>Psrb-6</i> F	tctacttttaaatattatattcttctaattttgcaacgaa
<i>Psrb-6</i> R	ttttatttctctgtagaaattcaagactgatca
<i>Pnmtn-1</i> F	gaaccaattgacataatgctctc
<i>Pnmtn-1</i> R	tttagcatggataatgttattgcg